

Spitzer reveals what's behind Orion's Bar

Robert H. Rubin^{1,2}, Janet P. Simpson^{1,3}, C. R. O'Dell⁴, Ian A. McNabb⁵, Sean W. J. Colgan¹, Scott Y. Zhuge¹, Gary J. Ferland⁶ and Sergio A. Hidalgo¹

robert.h.rubin@nasa.gov

October 3, 2018

ABSTRACT

We present *Spitzer* Space Telescope observations of 11 regions southeast of the Bright Bar in the Orion Nebula, along a radial from the exciting star θ^1 Ori C, extending from 2.6 to 12.1'. Our Cycle 5 programme obtained deep spectra with matching IRS short-high (SH) and long-high (LH) aperture grid patterns. Most previous IR missions observed only the inner few arcmin (the ‘‘Huygens’’ Region). The extreme sensitivity of *Spitzer* in the 10-37 μm spectral range permitted us to measure many lines of interest to much larger distances from θ^1 Ori C. Orion is the benchmark for studies of the interstellar medium, particularly for elemental abundances. *Spitzer* observations provide a unique perspective on the neon and sulfur abundances by virtue of observing the dominant ionization states of Ne (Ne^+ , Ne^{++}) and S (S^{++} , S^{3+}) in Orion and H II regions in general. The Ne/H abundance ratio is especially well determined, with a value of $(1.01 \pm 0.08) \times 10^{-4}$ or in terms of the conventional expression, $12 + \log (\text{Ne}/\text{H}) = 8.00 \pm 0.03$.

We obtained corresponding new ground-based spectra at Cerro Tololo Interamerican Observatory (CTIO). These optical data are used to estimate the electron temperature, electron density, optical extinction, and the S^+/S^{++} ionization ratio at each of our *Spitzer* positions. That permits an adjustment for the total gas-phase sulfur abundance because no S^+ line is observed by *Spitzer*. The gas-phase S/H abundance ratio is $(7.68 \pm 0.30) \times 10^{-6}$ or $12 + \log (\text{S}/\text{H}) =$

¹NASA/Ames Research Center, Moffett Field, CA 94035-1000, USA

²Orion Enterprises, M.S. 245-6, Moffett Field, CA 94035-1000, USA

³SETI Institute, 515 N. Whisman Road, Mountain View, CA 94043, USA

⁴Physics & Astronomy Department, Vanderbilt University, Box 1807-B, Nashville, TN 37235, USA

⁵Kavli Institute for Astronomy & Astrophysics, Peking University, Beijing, China

⁶University of Kentucky, Department of Physics & Astronomy, Lexington, KY 40506, USA

6.89±0.02. The Ne/S abundance ratio may be determined even when the weaker hydrogen line, H(7–6) here, is not measured. The mean value, adjusted for the optical S⁺/S⁺⁺ ratio, is Ne/S = 13.0 ± 0.6.

We derive the electron density (N_e) versus distance from θ^1 Ori C for [S III] (*Spitzer*) and [S II] (CTIO). Both distributions are for the most part decreasing with increasing distance. The values for N_e [S II] fall below those of N_e [S III] at a given distance except for the outermost position. This general trend is consistent with the commonly accepted blister model for the Orion Nebula. The natural shape of such a blister is concave with an underlying decrease in density with increasing distance from the source of photoionization.

Our spectra are the deepest ever taken in these outer regions of Orion over the 10-37 μm range. Tracking the changes in ionization structure via the line emission to larger distances provides much more leverage for understanding the far less studied outer regions. A dramatic find is the presence of high-ionization Ne⁺⁺ all the way to the outer optical boundary $\sim 12'$ from θ^1 Ori C. This IR result is robust, whereas the optical evidence from observations of high-ionization species (e.g. O⁺⁺) at the outer optical boundary suffers uncertainty because of scattering of emission from the much brighter inner Huygens Region. The *Spitzer* spectra are consistent with the Bright Bar being a high-density ‘localized escarpment’ in the larger Orion Nebula picture. Hard ionizing photons reach most solid angles well SE of the Bright Bar. The so-called Orion foreground ‘Veil’, seen prominently in projection at our outermost position 12' from θ^1 Ori C, is likely an H II region – photo-dissociation region (PDR) interface. The *Spitzer* spectra show very strong enhancements of PDR lines – [Si II] 34.8 μm , [Fe II] 26.0 μm , and molecular hydrogen – at the outermost position.

Subject headings: ISM: abundances, H II regions, individual (Orion Nebula)

1. Introduction

Most observational studies of the chemical evolution of the universe rest on emission line objects. H II regions help elucidate the current mix of elemental abundances in the ISM. They are laboratories for understanding physical processes in all emission-line sources and probes for stellar, galactic, and primordial nucleosynthesis. H II regions are also among the best tracers of recent star formation. The Orion Nebula (M42) is the benchmark for studies of the interstellar medium (ISM), particularly as a gauge of elemental abundances. In many ways this is similar to the role the Sun plays with respect to stars. Because Orion is nearby

and bright, it is one of the most observed nebulae. Not surprisingly, most observations of Orion have been of the inner bright region. [Here we refer to this inner region as the classical “Huygens Region”.] Detailed photoionization models, including our own (Baldwin et al. 1991; Rubin et al. 1991a, b) as well as deep spectroscopic observations interpreted via empirical analyses (Esteban et al. 2004; Baldwin et al. 2000) have concentrated on the Huygens Region.

The Bright Bar has been treated as the “poster child” H II region – photo-dissociation region (PDR) interface. The famous 3-colour image of the PDR (Tielens et al. 1993) demonstrated the progressive separation of the $3.3 \mu\text{m}$ polycyclic aromatic hydrocarbon (PAH) feature (blue), H_2 1-0 S(1) (green), and CO $J = 1-0$ (red) with increasing distance from θ^1 Ori C. This was in good agreement with their theoretical model of a plane-parallel slab for the Bright Bar. Their result showed conclusively that the incident far-UV (non-ionizing) radiation field from θ^1 Ori C was responsible for this molecular structure in the Bright Bar. Because their interest primarily concerned the structure, properties, and observations of the Bright Bar PDR, they were not concerned with the emission that extends far beyond in the extended Orion Nebula (obviously present, from any reasonably deep photograph). With regard to the Huygens Region, one of our own papers derived a 3-dimensional model of the inner ionized region (Wen & O’Dell 1995). This work used detailed surface brightness images to delineate the 3-dimensional position of the main ionization front with increasing distance from the exciting star θ^1 Ori C, and argued that the Bright Bar is almost perpendicular to the plane of the sky.

With regard to the fainter extended outer nebula, there has been progress in characterizing the so-called foreground “Veil” with early *prima facie* evidence for its existence stemming from the H I 21-cm line absorption line work of van der Werf & Goss (1989). The Veil is seen in projection (\sim edge-on) as the outer boundary of M42, the grayish colour extending from roughly north counter clockwise to the southeast in the optical image shown here as Figure 5. For a review of the structure of Orion, see O’Dell (2001) and references therein. More recent studies of the Veil include Abel et al. (2004 and 2006).

Using the *Kuiper Airborne Observatory (KAO)*, Simpson et al. (1986) measured the [O III] 51.8 and $88.4 \mu\text{m}$ lines at several positions in Orion along a radial straight south from θ^1 Ori C, extending as far as a position called P6 centred $3.75'$ from θ^1 Ori C. This did provide IR evidence of species as high ionization as O^{++} beyond the Bright Bar. Except as noted, prior to *Spitzer*, high spectral resolution space- or airborne-IR data have never extended to angular separations from θ^1 Ori C that would place them in the extended outer nebula. To the best of our knowledge, the first such data exterior to the Bright Bar and the Huygens Region were taken under the GTO 45 programme (PI: T. Roellig) and the

GO 1094 programme (PI: F. Kemper). We did not examine the GTO 45 spectra, (“Orion Bar neutral”), a pair of short-high resolution (SH) and long-high resolution (LH) aperture spectra centred close to and just SE of θ^2 Ori A, taken in staring mode. Instead, we chose to examine a set of the GO 1094 paired SH and LH aperture spectra centred well SE of the Bright Bar ~ 3.4 arcmin from θ^1 Ori C. These spectra were taken in staring mode with the minimum ramp (exposure) time of 6 s and total for each spectrum of just 12 s. As will be discussed later, the fields of view for the SH and LH were quite different. These spectra demonstrated that there were lines of high-ionization species ([Ne III] and [S IV]) measurable with excellent signal-to-noise even beyond the PDR of the Bright Bar. We also determined that none of the emission lines was saturated. Those 24 s of data were an inspiration for us to propose using *Spitzer* to probe even further from θ^1 Ori C.

Spitzer has a unique ability to address the abundances of the elements neon and sulfur. This is particularly true in the case of H II regions, where one can simultaneously observe four emission lines that probe the dominant ionization states of Ne (Ne⁺ and Ne⁺⁺) and S (S⁺⁺ and S³⁺). The four lines, [Ne II] 12.81, [Ne III] 15.56, [S III] 18.71, and [S IV] 10.51 μm can be observed cospatially with the Infrared Spectrograph (IRS) on the *Spitzer*. Because of the sensitivity of *Spitzer*, a special niche, relative to previous (and near-term foreseeable) instruments, is for studies of fainter H II regions. Indeed many of the well-known Galactic H II regions would cause saturation problems if observed at their brightest positions. Because of this, prior to our Orion programme, we have used *Spitzer* to observe a number of H II regions in galaxies with various metallicities and other properties. These studies were of the spiral galaxies M83 (Rubin et al. 2007, hereafter R07), M33 (Rubin et al. 2008, hereafter R08), and the dwarf irregular galaxy NGC 6822 (Rubin et al. 2010, hereafter R10). To the extent that all the major forms of Ne and S are observed, the true Ne/S abundance ratio could be inferred. For Ne, this is a safe assumption, but for S, there is the possibility of non-negligible contributions due to S⁺ as well as what could be tied up in dust.

We have an ongoing interest to utilize this special capability of *Spitzer* archival spectra to address the Ne/S abundance ratio. Our current assessment of how much Ne/S may vary was discussed in Rubin et al. (2008), where we also included other *Spitzer* data, reanalyzed with a homogeneous atomic database. In this paper, we make a careful assessment of the Orion Nebula value for Ne/S. This not only uses *Spitzer* measurements of the dominant ionic species, but also new ground-based spectra that permit an accounting for S⁺, which *Spitzer* cannot do. In the customary role of the Orion Nebula providing an important benchmark for the ISM, it is important to compare the Ne/S value with others, including the uncertain and controversial solar value as well as what is predicted by nucleosynthesis, galactic chemical evolution (GCE) models.

The solar abundance, particularly of Ne, remains the subject of much controversy (e.g., Drake & Testa 2005; Bahcall, Serenelli, & Basu 2006; and references therein). The preponderance of evidence points to a Ne abundance substantially higher in the solar neighborhood, and even in the Sun itself, than the “canonical” solar values, Ne/S \sim 6.5 (Asplund et al. 2009). While we cannot directly address the solar Ne value, it is crucial to an understanding of nucleosynthesis and GCE to have reliable benchmarks. We made the case that the solar Ne/S ratio is ‘out of line’ with our *Spitzer* H II region values (R07, R08, R10 and references therein). *Note that the reason abundances are often derived as ratios is to avoid absolute calibration problems.* Previous to that, Pottasch & Bernard-Salas (2006) discussed in their study of planetary nebulae with the *Infrared Space Observatory (ISO)* that the solar neon abundance was likely too low. They suggested that the planetary nebula neon abundance should be used instead. Optical studies of planetary nebulae and H II regions have suggested an upward revision of the solar Ne/O ratio (Wang & Liu 2008; Magrini, Stanghellini, & Villaver 2009). Recent observations of nearby B stars also suggest that the solar Ne/O ratio should be higher (e.g., Morel & Butler 2008).

With our new Orion data, we focus predominantly on neon, the fifth most abundant element in the Universe, and sulfur, one of the top ten, because of the specific capability that *Spitzer* provided. Naturally, deriving abundances of other elements is also important, but there was no special ability to tackle these with *Spitzer*. Suffice it to say that to provide precision abundance measurements of S and Ne is a major advance in basic data needed to understand and test nucleosynthesis/GCE models. While both S and Ne are ‘primary’ α -elements produced in massive stars and released to the ISM in supernovae, some differences in their production and GCE may be expected. ^{20}Ne exists primarily in the C-burned shell of massive stars, whereas ^{32}S arises during O-burning, probably explosively (e.g., an interesting article with a useful cutaway schematic of the fusion zones by Clayton 2007). According to figure 7 in the nucleosynthesis/GCE model of Woosley & Heger (2007), the Ne/S ratio is \sim 8.6, when they start with the Lodders (2003) solar abundances.

We discuss the *Spitzer* observations in section 2. In section 3, our new ground-based spectra are presented. In section 4, we discuss the variation of the electron density and three measures of the degree of ionization with distance from the exciting star. Section 5 continues with the derivation of elemental abundance ratios: Ne/S, Ne/H, S/H, and Fe/H. In section 6, we present additional data in order to characterize the Bright Bar and Outer Veil in the context of an overview of the entire Orion Nebula. In section 7, there is additional discussion pertaining to the major findings, including the Ne/S & Ne/H ratios and the nature of the Bright Bar and Outer Veil as an H II region – PDR interface. Last, we provide a summary and conclusions in section 8.

2. *Spitzer Space Telescope Observations*

We observed the outer Orion Nebula under our Cycle 5 *Spitzer Space Telescope* programme GO-50082. The observations were all southeast of the famous bar, which we shall refer to as the Bright Bar (BB). The fields chosen were centred along a radial outbound from the exciting star θ^1 Ori C and approximately orthogonal to the BB (see Figure 1). This radial coincides with our “Slit 4”, one of the slits defined in our previous programme with *HST/STIS* long-slit spectra. The SE tip passed through HH203 (Rubin et al. 2003, colour fig. 1). Our set of positions was selected to examine the far side of the Bright Bar. There are 11 locations that start at $2.6'$ and extend to $12.1'$ from θ^1 Ori C (see Figure 1). In order of increasing distance (D) from θ^1 Ori C, the positions are called “inner” (I4, I3, I2, I1), “middle” (M1, M2, M3, M4), and “veil” (V1, V2, V3). Table 1 lists the coordinates for the centres of the areas mapped and the projected angular distance D. We note that for the inner positions, the time-sequence order of observations was indeed I1, I2, I3, and I4. We chose that just in case the brightest I4 region might suffer some saturation effect, which might then cause a latency problem with the subsequent observation position. Fortunately, we experienced no saturation issues.

We obtained deep spectra with both the *Spitzer* Infrared Spectrograph (IRS) short wavelength, high dispersion (spectral resolution, $R \sim 600$) configuration, called the short-high (SH) module and the long wavelength, high dispersion ($R \sim 600$) configuration, called the long-high (LH) module (e.g., Houck et al. 2004). These cover respectively the wavelength range from $9.9 - 19.6 \mu\text{m}$ and from $\sim 19 - \sim 36 \mu\text{m}$. The SH slit size is $4.7'' \times 11.3''$, while the LH is $11.1'' \times 22.3''$. The SH observations permit cospatial observations of five important emission lines: [S IV] 10.51, hydrogen H(7–6) ($\text{H}\alpha$) 12.37, [Ne II] 12.81, [Ne III] 15.56, and [S III] 18.71 μm . The LH observations permit cospatial observations of several more important emission lines: [Fe III] 22.93, [Fe II] 25.99, [S III] 33.48, [Si II] 34.82 μm . In order that we could use **all** the emission lines observed with both modules, we made a concerted effort to match the field of view (FOV) for the SH and LH modules. However, a perfect match is not possible because the SH and LH rectangular apertures are not exactly orthogonal (84.8°). With the “mapping mode” for the IRS, we had the ability to overlap apertures by offsetting in either the parallel direction (along the long-axis of the rectangular aperture) or the perpendicular direction (along the short-axis of the aperture). By selecting the following scheme, the resulting SH and LH aperture grid patterns (henceforth ‘*chex*’, after the breakfast cereal) very closely match the same area in the nebula: with SH, one displacement of $5''$ parallel and 9 displacements of $2.3''$ perpendicular; with LH, one displacement of $4.5''$ parallel and one displacement of $4.5''$ perpendicular. We used the *Spitzer* software SPOT to measure our chex size. The SH is $25.4'' \times 16.3''$ (area 414.0 arcsec²) and the LH is $26.8'' \times 15.5''$ (area 415.4 arcsec²), indeed a good match (see Figure 1). Another very important purpose of

overlapping the apertures is that most spatial positions will be covered in several locations on the array, minimizing the effects of bad pixels.

To save overhead, we clustered our 11 positions into 5 on-source *Spitzer* Astronomical Observing Requests (AORs). Because much more integration time was necessary to observe the fainter veil positions (V1, V2, V3 – all three included in the *same* AOR), we needed to split these into 3 separate AORs, that were designated veil1, veil2, and veil3. The other two AORs clustered all of the inner positions in one and all the middle positions in the other. We did not control the scheduling of the AORs which were actually in the following time sequence (with the data set number, and total time in min.): veil3 (25381120, 261.94); middle (25381362, 276.97); inner (25381376, 198.80); veil2 (25380864, 261.96); and veil1 (25380608, 326.37). For various reasons, we **changed the nomenclature** herein for the three veil data sets – veil1, veil2, and veil3 refer to respective data sets 25380864, 25380608, and 25381120. Throughout this paper Vx-y means chex x and AOR y. For example, V3-1 means chex V3 and veil AOR 1 (data set 25380864).

The entire programme was executed between 2008 November 14 and November 21 (UT), thereby causing very little sky-rotation of the FOV. Immediately adjacent in time to each on-source AOR, a background off-source AOR was taken. These were all done at the same position – $\alpha, \delta = 5^{\text{h}}32^{\text{m}}36^{\text{s}}.5, -5^{\circ}17'47''$ (J2000) – in “staring mode”, which utilizes a single aperture with a shift along the long-slit axis (parallel direction) of 1/3 the aperture dimension. More time was used to observe those background observations associated with the fainter regions. Our choice of ramp (exposure) times and number of mapping cycles was as follows: inner chex, SH 6 s, 8 cycles and LH 6 s, 8 cycles; middle chex, SH 6 s, 12 cycles and LH 14 s, 6 cycles; for all veil chex, SH 30 s and LH 14 s. For both AORs veil2 and veil3, there were 5 and 11 cycles respectively for the SH and LH, while more time was used in veil1 with 6 and 17 cycles respectively to fill up our *Spitzer* allotment.

Our data were processed and calibrated with version S18.5 of the standard IRS pipeline at the *Spitzer* Science Center. To build our post-BCD (basic calibrated data) data products, we use CUBISM, the CUbe Builder for IRS Spectral Mapping, (version 1.6) (Smith et al. (2007a, b and references therein). CUBISM was used to build maps, which account for aperture overlaps, and to deal effectively with bad pixels. From the IRS mapping observations, it can combine these data into a single 3-dimensional cube with two spatial and one spectral dimension. For each of our regions, we constructed a data cube. Global bad pixels (those occurring at the same pixel in every BCD) were removed manually. Record level bad pixels (those occurring only within individual BCDs) – that deviated by 5σ from the median pixel value and occurred within at least 10 per cent of the BCDs – were removed automatically in CUBISM with the “Auto Bad Pixels” function. In reducing our data, we were careful to

ensure that the “Auto Bad Pixels” function did not incorrectly flag any of the pixels on our programme spectral lines as bad. Our Orion chex are in a fairly “smooth” area, and as such, it is more appropriate to reduce our data assuming each region is uniformly extended within the SH and LH apertures. This is the default option and the one we used with CUBISM.

The fully processed background-subtracted spectra that we use are presented in a colour montage showing all 11 chex in Figure 2 for the SH and Figure 3 for the LH. For the veil chex, we show only the longest-exposure spectra (the one formed from data set 25380608) in order not to clutter the figures. These figures provide a useful overview of the changes that occur at the varying distances from the exciting star. The changes to the continuum levels and the PAH features can also be seen. For instance, it is apparent that the continuum intensity decreases with increasing distance from θ^1 Ori C from I4 through V1, but then increases from V1 to V3. All of the spectral lines that we discuss in the paper are labeled in Figures 2 and 3. There are some features that we do not measure or discuss that are also labeled. These include the PAH bands and weaker lines such as H(8-7). In addition, the very recently identified C_{60} feature near $18.9 \mu\text{m}$ (Cami et al. 2010) is also marked. They found this in the young planetary nebula Tc 1 and as they discuss, a minor fraction of this emission feature is due to C_{70} also.

Our further analysis of these spectra used the line-fitting routines in the IRS Spectroscopy Modeling Analysis and Reduction Tool (SMART, Higdon et al. 2004). The emission lines were measured with SMART using a Gaussian line fit. The continuum baseline was fit with a linear or quadratic function. Figures 4 (a)–(d) show the data and fits for several lines at chex V3 for one of the three veil AORs, the one we call veil1 (using data set 25380864). Most of our line measurements have higher signal-to-noise (S/N) than these. We display this set to illustrate that lines from species as highly ionized as Ne^{++} are clearly measurable all the way to the outer extended optical boundary.

A line is deemed to be detected if the intensity is at least as large as the 3σ uncertainty. We measure the uncertainty by the product of the full-width-half-maximum (FWHM) and the root-mean-square variations in the adjacent, line-free continuum; it does not include systematic effects. The possible uncertainty in the absolute flux calibration of the spectroscopic products delivered by the pipeline is likely confined to between 5 and 10 per cent (see discussion on p. 1411 of R07). Any uncertainty in the flux due to pointing errors is probably small and in the worst case should not exceed 10 per cent. For the brighter lines the systematic uncertainty far exceeds the measured (statistical) uncertainty. Even for the fainter lines, we estimate that the systematic uncertainty exceeds the measured uncertainty. In addition to the line intensity, the measured FWHM and heliocentric radial velocities (V_{helio}) are listed in Table 2. Both the FWHM and V_{helio} are useful in judging the reliability of the line mea-

surements. The FWHM is expected to be the instrumental width for all our lines. With a resolving power for the SH and LH modules of ~ 600 , our lines should have a FWHM of roughly 500 km s^{-1} . The values for V_{helio} should straddle the heliocentric systemic radial velocity for M42. For the Huygens Region, heliocentric velocities of the higher ionization lines are $\sim +18 \text{ km s}^{-1}$, those for the lower-ionization species near the main ionization front are $\sim +25 \text{ km s}^{-1}$, while those for the PDR lines are $\sim +28 \text{ km s}^{-1}$ (O’Dell 2001). Subject to the coarse spectral resolution with *Spitzer*, most of our measurements are in agreement with these expectations.

3. Ground-based Observations

The ground-based spectroscopy was performed with the Boller & Chivens spectrograph mounted on the 1.5 m telescope at the Cerro Tololo Interamerican Observatory on the nights of 2008 November 18, 19, 22, 24 and 2009 December 9, 10, 13 (UT). Observations were made with a long slit crossing at or near most of the positions measured with *Spitzer*. The illuminated portion of the $2.6''$ wide slit was $429''$ long in the 2008 observations and $345''$ during the 2009 observations. The slit was opened to greater than $5''$ width during observations of the photometric reference stars Feige 15, Feige 25, and Hiltner 600, which was wide enough to include all of the wavelengths measured over the limited range of zenith distances (25° to 51°) employed and the astronomical seeing image size of no more than $1.0''$. Feige 15 observations were made early each night at multiple zenith distances in 2008 and multiple reference stars were observed once each night in 2009. Photometrically clear conditions applied during all observations of the reference stars and the nebula.

All observations were made such that the first order of the grating was employed with a chopping filter (GG 385 in 2008 and GG 395 in 2009) that permitted measurement of the red end of the spectrum without contamination by signal from the overlapping second order. Each pixel of the Loral 1K CCD subtended $1.30''$ along the slit. For the 400 lines/mm (blaze 8000 \AA) grating 58 observations on the first three nights in 2008 (November 18, 19, 22), each pixel along the dispersion was about 2.2 \AA and the FWHM of the emission lines was about 6.7 \AA . The 300 lines/mm, blaze 4000 \AA grating 09 used on the night of 2008 November 24 and for the 2009 observations gave a slightly higher wavelength range, had a scale of 2.9 \AA per pixel, and $\text{FWHM} = 6.8 \text{ \AA}$. A position angle (PA) of 134.6° was used for observations centring the star JW 831 (Jones & Walker 1988) and $\text{PA} = 59.9^\circ$ used for JW 873. On the third night in 2008 the $\text{PA} = 90^\circ$ slit was placed $11.7''$ south of JW 887, while on the fourth night of 2008 the $\text{PA} = 90^\circ$ slit was carefully displaced to the south from the brightest Trapezium star $\theta^1 \text{ Ori C}$ distances of $120''$, $150''$, and $180''$. During the 2009

observations, JW 887 was used for displacements to positions V1 and M4, and JW 975 was used for the displacement to V3. The location of the slits are shown in Figure 5.

Sky observations were made at two locations selected to be well removed from nebular emission, these being identified from wide field of view $H\alpha+[N II]$ images of the region. The sky positions were $\alpha, \delta = 5^h26^m03^s, -0^\circ25'42''$ and $5^h28^m19^s, -7^\circ08'36''$ (J2000) and the measurements were indistinguishable from one another. In 2008 on the first night of the JW 831 observation of a bright portion of the nebula, sky observations totaling 3600 seconds were made. On the second night of the JW 873 observations, sky observations totaling 2700 seconds were made. On the third night of the JW 887 observations, four sky observations totaling 3600 seconds were made, and on the fourth night of the observations displaced from θ^1 Ori C, frequent observation sets of 2400 seconds were interleaved with the observations of the nebula. In 2009, 3600 seconds of sky observations were made on December 9 and 7200 seconds of sky observations on each of December 10 and 13. Observations of the twilight sky were made and used to determine the illumination correction along the slit.

Where necessary, a series of exposure times were used since the strongest emission-lines entered the non-linear portion of the CCD detector during the long exposures. In all cases the exposures were made in pairs, which were then used for correction of cosmic-ray tracks. For the JW 831 observations, twin exposures of 60, 300, 600, and 1200 seconds were made. For the JW 873 observations, twin exposures of 600 seconds and two twin exposures of 1800 seconds were made. For the JW 887 observations twin exposures of 900 seconds were made. For the fourth night observations displaced south from θ^1 Ori C, exposure times were 60 seconds for $120''$, 120 seconds for $150''$, and 150 seconds for $180''$. The total signal per pixel along the slit in the $H\beta$ reference line ranged from 2200 to 7200 analog-digital-units (ADU) at a gain of 0.7 ADU per electron event for the shortest exposures in the faintest to brightest regions sampled. In the case of the V1, V3, and M4 observations in 2009, total exposure times of 3900 seconds, 5700 seconds, and 3900 seconds were used. IRAF¹ tasks were used to process and spectro-photometrically calibrate the observations.

Samples from along the slits that correspond to different *Spitzer* observations were taken. The location of the sampled regions are also shown in Figure 5. The total intensity in each emission-line was measured by fitting each line with a Lorentzian line profile using the task ‘*splot*’. Features that were identified as a blend of emission from two or more ions, using the high spectral resolution results of Esteban et al. (2004) as a guide, were not measured.

¹IRAF is distributed by the National Optical Astronomy Observatories, which is operated by the Association of Universities for Research in Astronomy, Inc. under cooperative agreement with the National Science foundation.

All the measured line intensities were then normalized to $H\beta$. A representative spectrum is shown in Figure 6. Because of the wide range of intensities, this M4 position spectrum is shown as a logarithm of the intensity.

The effects of interstellar extinction were removed by comparing the observed $H\alpha/H\beta$ flux ratio with the value of 2.89 expected from recombination theory assuming case B, electron density (N_e) = 1000 cm^{-3} , and electron temperature (T_e) = 8500 K (Storey & Hummer 1995), and employing the recently determined reddening curve derived by Blagrove et al. (2007) from the nebular He I lines. Note that the predicted $H\alpha/H\beta$ flux ratio changes little with N_e and T_e over our range of interest. The results are expressed as the commonly used logarithmic extinction at $H\beta$ ($c_{H\beta}$) and are given in Table 3. This table also gives the extinction corrected surface brightness of the sample in the $H\beta$ line. Tables 4 – 7 present the observed (F_λ) and extinction corrected (I_λ) line intensities relative to $H\beta$ for the 16 different spectral samples. In the case of the southwest-most samples, the observed $H\alpha/H\beta$ ratios were less than theoretically expected. The theoretical $H\alpha/H\beta$ ratios vary only slowly with T_e and matching the observations would require temperatures twice as high as those derived from heavy ion line ratios. The dominance of higher temperatures in the $H\alpha$ and $H\beta$ emitting regions is probably not the correct interpretation of these data because hydrogen recombination emission increases with decreasing T_e . Thus this emission should selectively come from any lower T_e regions along the line of sight.

The explanation of these anomalously low $H\alpha/H\beta$ ratios probably lies with the fact that these regions have important components of the emission illuminated from the much brighter part of the nebula that are being scattered by material along these outer lines of sight. One knows from high spectral resolution studies (O’Dell 1992, Henney 1994, Henney 1998, O’Dell 2001) that even in the inner nebula, the dust component of the PDR beyond the main ionization front scatters several tens of per cent of the emission and that the nebular continuum (Baldwin et al. 1991) is much stronger than expected for an atomic continuum because of scattered light from the Trapezium stars. The anomalously low line ratio would indicate that the bluer $H\beta$ line is scattered more efficiently than the $H\alpha$ line. Since the effects of such scattering have not been modeled and there is a pattern of decreasing extinction in the direction of the anomalous line ratios, we have assumed that there is no extinction in those four samples. This assumption and the uncertainties of the role of the scattered emission-line radiation probably introduce an uncertainty of the derived line ratios of about 10 per cent.

Electron temperatures were determined from line ratios using the IRAF-STSDAS task TEMDEN from the [N II] ratio $[I(6548) + I(6583)]/I(5755)$ and the [O III] ratio $[I(4959) + I(5007)]/I(4363)$. Electron densities were determined using the [S II] $I(6716)/I(6731)$ ratios

but *updating* the atomic data as discussed in the next section. These combinations give the particularly useful advantage of sampling different regions along the line of sight. [S II] emission will arise essentially at the main ionization front, [N II] emission comes from a zone where hydrogen is ionized and helium is neutral, and the [O III] emission comes from a zone where H is ionized and He is singly ionized (O’Dell 1998). The results of the calculations are presented in Table 8.

4. Variations with Distance from the Exciting Star

4.1. Variations in Electron Density

The *Spitzer* data provide an excellent diagnostic of electron density (N_e) in the S^{++} region from the line flux ratio [S III] 18.7/33.5 μm . Likewise, the ground-based observations provide an excellent diagnostic of N_e in the S^+ region from the line flux ratio [S II] 6716/6731 \AA . Both of these diagnostic tools are very insensitive to T_e (e.g., Rubin 1989). For our analyses, we will use $T_e = 8000$ K. The optical spectra discussed in the last section permit an assessment of T_e [N II] and T_e [O III] values (see Table 8) from classical forbidden line ratios. While these values for T_e are somewhat higher than the 8000 K adopted, we point out a well-known bias. That is, both T_e [O III] and T_e [N II] derived from the ratio of fluxes of ‘auroral’ to ‘nebular’ lines are systematically higher than the so-called ‘ T_0 ’, which is the $(N_e \times N_i \times T_e)$ -weighted average, where N_i is the ion density of interest. The amount of this bias depends on the degree of T_e variations in the observed volume (see Peimbert 1967, and many forward references). In our analyses, for N_e now, and in later sections using the set of IR lines, it is more appropriate to be using a T_e that is similar to T_0 . Because of the insensitivity of the volume emissivities to T_e , particularly when working with ratios for these IR lines, our results depend very little on this T_e choice.

Figure 7 shows N_e [S III] and N_e [S II] versus D (the projected distance in arcmin from θ^1 Ori C to the centre of the chex or optical sample). For [S III], we use the effective collision strengths from Tayal & Gupta (1999) and the transition probabilities (A-values) from the recent compilation “Critically Evaluated Atomic Transition Probabilities for Sulfur S I – S XV” (Podobedova, Kelleher & Wiese 2009). The original source they cite is Froese Fischer, Tachiev & Irimia (2006). For [S II], we use the effective collision strengths from Ramsbottom, Bell & Stafford (1996) and the A-values from Podobedova et al. (2009) with the original source Irimia & Froese Fischer (2005).

These two N_e distributions provide a unique perspective for the extended outer Orion Nebula. Clearly the values for N_e [S II] fall below those of N_e [S III] at a given D except

for the outermost regions, including V3. For any given *Spitzer* chex or optical sample, we view a column along the line of sight with a rectangular cross section. Due to ionization stratification, S^{++}/S^+ will be selectively highest in the column near the minimal projected distance from θ^1 Ori C. Along this line-of-sight, at distances on either side of the minimum impact parameter, S^{++}/S^+ will be expected to be decreasing because the actual 3-D distance to θ^1 Ori C is larger. In this picture, there would not be a plane-parallel density profile but one that had a degree of concavity with respect to θ^1 Ori C and an approximately monotonically decreasing density with increasing D from the exciting star.

There are several other considerations. A blister is not only the commonly accepted model for the Orion Nebula, it is also a natural configuration once a nebula enters the champagne-phase (e.g., Tenorio-Tagle 1979). Ionizing radiation leads to the creation of a dense PDR and an ionization stratified layer facing the dominant ionizing source (θ^1 Ori C). The natural shape of such a blister is concave, thus explaining the general form of the Huygens Region (Wen & O’Dell 1995). The factors that produce the concavity in the Huygens Region will also be at play further away as one gets beyond the perturbation of the Bright Bar. In quasi-steady state, there would be a gas density drop going away from the PDR into the ionized layer.

When viewing [S II] emission, we are seeing material that is for the most part very close to the H^+-H^0 ionization front. Just interior to this H-ionization front is where sulfur transitions from S^{++} to S^+ . There is then the possibility that the bulk of the [S II] emission arises from a region where there is only partial ionization of hydrogen. Hence N_e as measured by N_e [S II] would be lower than that obtained from N_e [S III] even though the *total* gas density could be higher (as the PDR is approached) than the total gas density nearby, but closer to θ^1 Ori C.

In order to explain why N_e [S II] exceeds N_e [S III] at the outermost position V3, we offer the following. As one views far enough away from θ^1 Ori C, scattered light becomes more important. By comparing $H\beta$ and the radio continuum, O’Dell & Goss (2009) showed that in the outer Orion regions the dust in the PDR is not only scattering Trapezium optical starlight, but also scattering nebular emission line radiation produced in the much brighter Huygens Region. While this can be important for the [S II] emission, the infrared [S III] emission will be far less affected by scattering. The optical spectrum at V3 has a strong continuum, indicating substantial scattered optical light. This is likely why N_e [S II] is larger than N_e [S III] because the [S II] flux is a mix of local (low N_e) emission and scattered light from the higher N_e Huygens Region.

4.2. Variations in Degree of Ionization

From the measured infrared intensities, we are able to estimate ionic abundance ratios for three elements in adjacent ionic states: $\text{Ne}^{++}/\text{Ne}^+$, $\text{S}^{3+}/\text{S}^{++}$ and $\text{Fe}^{++}/\text{Fe}^+$. Important advantages compared with optical studies of various other ionic ratios are: (1) the IR lines have a weak and similar T_e dependence, while the collisionally-excited optical lines vary exponentially with T_e (e.g., Osterbrock & Ferland 2006), and (2) the IR lines suffer far less from interstellar extinction and scattering. Indeed for our purposes, the differential extinction correction is negligible as the lines are relatively close in wavelength. In our analysis, we deal with ionic abundance ratios and therefore line intensity ratios. In order to derive the ionic abundance ratios, we perform the usual semiempirical analysis assuming a constant T_e and N_e to obtain the volume emissivities for the pertinent transitions. We use the atomic data described in Simpson et al. (2004) and Simpson et al. (2007) except for the A-values for the sulfur ionic species. Earlier we discussed [S III] and [S II]. We also use the A-values in Podobedova et al. 2009 for [S IV]. The original source they cite is ‘Froese Fischer 2002a, downloaded from <http://atoms.vuse.vanderbilt.edu/> on 2005 December 21’. In addition, we use a different effective collision strength for the [Ne II] line, as detailed in the next paragraph.

4.2.1. $\text{Ne}^{++}/\text{Ne}^+$

We present both the variation of the observed flux ratio $F(15.6)/F(12.8)$ and $\text{Ne}^{++}/\text{Ne}^+$ with D in Figure 8 using the values from Table 2 and Table 10, respectively. Here and throughout, the error values represent the propagated intensity measurement uncertainties and do not include the systematic uncertainties. In this paper, we commence to use the effective collision strengths for [Ne II] of Griffin et al. (2001).² In our previous papers (R07, R08, and R10), we had used the values from Saraph & Tully (1994). Compared to those, the Griffin et al. values are approximately 10 per cent higher at the T_e ’s characteristic of H II regions. The Griffin et al. (2001) values appear to be the best available now (as also judged by Witthoef et al. 2007). We continue to use the same effective collision strengths for [Ne III] (McLaughlin & Bell 2000).

In our empirical derivation of ion ratios, as already discussed, we use the derived N_e [S III] and $T_e = 8000$ K throughout. The $F(15.6)$ decreases monotonically with D by

²The value at 8000 K is 0.310 from the more complete set of effective collision strengths, available on the Controlled Fusion Atomic Data Center Web Site at ORNL, www-cfadc.phy.ornl.gov/data_and_codes.

almost a factor of 700 from I4 to V3. We note that F(12.8) is a monotonically decreasing relation as well except for a rise at V2 of ~ 30 per cent compared with V1. Even though Ne^+ is the dominant neon ion beyond the Bright Bar, the [Ne III] 15.6 line is clearly present all the way to the outer boundary (see Figure 4). In fact, there is a very dramatic increase in the $\text{Ne}^{++}/\text{Ne}^+$ ratio for all three V3 observations by a factor of ~ 4.8 over the three V2 observations. The main reason for this jump is likely due to the large drop in N_e [S III] by a factor of 3 from V2 to V3. Ionization equilibrium dictates that $\text{Ne}^{++}/\text{Ne}^+ \propto N_e^{-1}$ all other things being equal. Whether the rest of the decrease in the neon ionization equilibrium (factor of ~ 4.8) is necessary to attribute to other causes is difficult to determine. We could speculate that there might be another source of hard ionizing photons besides θ^1 Ori C at this outer boundary, perhaps even external to the Orion Nebula.

4.2.2. $\text{S}^{3+}/\text{S}^{++}$

As for neon, we present both the variation with D of the observed flux ratio F(10.5)/F(18.7) as well as the derived ionic ratio $\text{S}^{3+}/\text{S}^{++}$ (Figure 9). Both [S IV] 10.5 and [S III] 18.7 intensities decrease monotonically with D. Clearly F(10.5) decreases more steeply than F(18.7) with increasing D. The [S IV] 10.5 line was detected in just one of the three V3 observations, V3-2. As for the $\text{Ne}^{++}/\text{Ne}^+$ ratio, the analysis shows that there is a similar dramatic increase in the $\text{S}^{3+}/\text{S}^{++}$ ratio for V3-2 by more than a factor of 5 over the V2 observations. The reasons provided in the last subsection would have a bearing for this ionic ratio as well. Following Table 2, we show non-detections in the plots as 3σ upper limits.

4.2.3. $\text{Fe}^{++}/\text{Fe}^+$

By virtue of the simultaneous measurement of both [Fe III] 22.9 and [Fe II] 26.0 lines with the LH module, the line flux ratio covers exactly the same sky area (as did ratios involving lines observed with the SH module). Here we present both the variation with D of the observed flux ratio F(22.9)/F(26.0) and the derived ionic ratio $\text{Fe}^{++}/\text{Fe}^+$ (Figure 10). Both [Fe III] 22.9 and [Fe II] 26.0 intensities decrease with increasing D except that there is a dramatic increase in F(26.0) at V2 by a factor of 2.2 compared to the intensity at V1. An increase was also noted above for the [Ne II] 12.8 line intensity. The [Fe III] 22.9 line was not detected in any of the three V3 observations and is treated as a 3σ upper limit in the plot. In Figure 10, the observed ratio F(22.9)/F(26.0) follows a very different pattern with D than those seen in Figures 8 and 9 with the higher ionization line in the numerator

and the lower ionization line in the denominator. The primary reason for this is that the [Fe II] 26.0 line has a very substantial PDR contribution (Kaufman et al. 2006), because it arises from the second energy level just 385 cm^{-1} above ground (e.g., see discussion on p. 1126 of Simpson et al. 2007). Our analysis of the $\text{Fe}^{++}/\text{Fe}^+$ ratio *does not account* for the PDR contribution to the [Fe II] 26.0 line intensity. We derive Fe^+ by assuming the 26.0 line intensity is excited by electron collisions only. Even for this excitation route, we have not accounted for the PDR contribution, which occurs at the lower $T_e \sim 500 \text{ K}$ for the upper (second) energy level. Thus the $\text{Fe}^{++}/\text{Fe}^+$ ratios derived using our measured [Fe II] 26.0 line intensity must be **lower limits**.

There is another [Fe II] line ${}^4F_{7/2} - {}^4F_{9/2}$ at $17.936 \mu\text{m}$ that has a purer H II region origin. This arises from a level 2430 cm^{-1} above ground (characteristic temperature $\sim 3500 \text{ K}$). Unfortunately, this is a weak line and at the SH spectral resolution, blended with [P III] ${}^2P_{3/2} - {}^2P_{1/2}$ at $17.885 \mu\text{m}$ (see Figure 2). We are able to measure this [Fe II] line only at chex V1 and V2. At V1 the [P III] line is the brighter while at V2 the [Fe II] line becomes the brighter. The $\text{Fe}^{++}/\text{Fe}^+$ ratio derived using this weak line is also shown in Figure 10 as the star symbol (red in the colour version). As expected, these few $\text{Fe}^{++}/\text{Fe}^+$ values are much higher than those inferred using the $26.0 \mu\text{m}$ line and should be considered the truer estimate of the $\text{Fe}^{++}/\text{Fe}^+$ ratio.

Figure 10 may hold some important clues about the behaviour of the outer Orion regions. Notable compared with the neon and sulfur plots is the increase in both $F(22.9)/F(26.0)$ and $\text{Fe}^{++}/\text{Fe}^+$ beginning from I2 to I1 (between $D = 3.7 - 4.4'$). While *both* $F(22.9)$ and $F(26.0)$ are decreasing with D for all the inner and middle chex, between I2 and I1, the drop in $F(26.0)$ is much larger (factor of 2.27) than that for $F(22.9)$ (factor of 1.25). The lower $F(22.9)/F(26.0)$ ratios at I4, I3 and I2 may be due to some residual influence of the Bright Bar contributing significantly to $F(26.0)$, although I2 is well removed from the BB. Another factor that may contribute to the ‘inversion’ in $F(22.9)/F(26.0)$ with D is the decrease in N_e . Again, ionization equilibrium would require that $\text{Fe}^{++}/\text{Fe}^+ \propto N_e^{-1}$, all other things being equal. Finally, another possibility that might contribute to the increased $F(22.9)/F(26.0)$ ratio between I2 to I1 is the presence of [Fe IV]. In fact, [Fe IV] is believed to be the most abundant ion in the Orion Nebula according to detailed photoionization models (Rubin et al. 1991a, 1991b; Baldwin et al. 1991). The discovery of the [Fe IV] 2837 \AA line in Orion (Rubin et al. 1997) was used to estimate the iron abundance. A more recent discussion may be found in Rodríguez & Rubin (2005). If the transition from Fe^{3+} to Fe^{++} is occurring between chex I2 and I1, this would help to explain the ‘inversion’.

5. Determination of Elemental Abundance Ratios

In this section we derive several ratios of elemental abundances that may be addressed with our *Spitzer* data. As stated earlier, we have been particularly interested in the Ne/S ratio and have undertaken several studies to utilize the special ability of *Spitzer* spectroscopy in this regard (R07, R08, R10). In this section, we first cover Ne/S. Then we derive and discuss three measures of metallicity: Ne/H, S/H and Fe/H.

5.1. Neon to Sulfur abundance ratio

For H II regions, using *Spitzer* data only, the gas-phase Ne/S ratio may be approximated as $(\text{Ne}^+ + \text{Ne}^{++})/(\text{S}^{++} + \text{S}^{3+})$. This includes the dominant ionization states of these two elements. However this relation does not account for S^+ , which should be present at some level. We may safely ignore the negligible contributions of neutral Ne and S in the ionized region. Figure 11 shows our approximation for Ne/S versus D.

Our ground-based observations, which cover [S II] 6716, 6731 Å and [S III] 6312 Å cospatially, allow for a correction to the *Spitzer*-data-only measurements. In order to estimate the downward corrections that apply to the individual chex, we derive S^+/S^{++} from the above optical lines. Because the position of the spectral long-slit sample extractions are usually not the same as the chex and always a much smaller area on the sky, we use the *optical sample closest to the various chex*. The volume emissivities used in conjunction with the extinction-corrected intensities for the [S II] 6716, 6731 and [S III] 6312 lines are those for N_e [S II] and N_e [S III] respectively; we continue to use $T_e = 8000$ K for both. With these S^+/S^{++} values, we correct the *Spitzer*-data-only estimate to obtain $\text{Ne/S} = (\text{Ne}^+ + \text{Ne}^{++})/(\text{S}^+ + \text{S}^{++} + \text{S}^{3+})$.

The derived S^+/S^{++} ratio is always less than 0.19 for any of the inner or middle chex. For the three sets of observations of the veil chex, it is no higher than 0.44. Thus S^{++} remains the dominant S ion even in the outermost regions. While we find a fairly constant Ne/S for the 8 chex comprising I4 – M4, Figure 11 indicates a steep increase in Ne/S with D in the veil positions. We surmise that this may be due to a significant and increasing amount of S being tied up in dust grains. It is a safe assumption that there will be negligible Ne in grains. Thus while the gas-phase Ne/S ratio may indeed be larger for these veil positions, the values presented in Figure 11 must be considered *upper limits for the total* Ne/S abundance ratio. Because of the likelihood that not all forms of a significant amount of sulfur are accounted for in the veil positions, our best estimate of the true Ne/S abundance ratio for the Orion Nebula is obtained from the eight values, corrected for S^+ , for the I4 – M4 chex. The median

value is 12.8. From the internal scatter amongst these 8 values, we obtain a sample mean and variance of 13.01 ± 0.64 . The uncorrected median for these same 8 chex is 15.0.

5.2. Ne/H and S/H

By virtue of measuring the H(7–6) line in the same SH spectra as the two neon and two sulfur lines, we are able to derive the Ne/H and S/H abundances. The H(7–6) line provides a measure of H^+ from recombination theory (Storey & Hummer 1995). There is a bit of a complication here because at Spitzer’s spectral resolution, the H(7-6) line is blended with the H(11-8) line. Their respective $\lambda(\text{vac}) = 12.371898$ and $12.387168 \mu\text{m}$. In order to correct for the contribution of the H(11-8) line, we use the relative intensity of H(11-8)/H(7-6) from recombination theory (Storey & Hummer 1995) assuming case B and $N_e = 500 \text{ cm}^{-3}$. The ratio H(11-8)/H(7-6) = 0.122 and holds over our range of interest $N_e = 100 - 1000 \text{ cm}^{-3}$ and $T_e = 8000 \text{ K}$. Indeed, it is appropriate for $T_e = 10000 \text{ K}$ and for case A as well.

There is also the possible blending with the H(7-6) line by He(7-6), that we do not account for in this paper, but now discuss with regard to how this would affect our analysis of metallicity. In an *ISO* short wavelength spectrometer (SWS) IR spectrum of the inner Orion Nebula (within the Huygens Region), the spectral resolution ($R \sim 2000$) permitted a separation of the H(5-4) from the strongest He(5-4) components (Rubin et al. 1998). They were then able to derive a robust He^+/H^+ ratio of 0.085 ± 0.003 from those H and He Br α transitions. In the present case, all the strongest fine-structure components of the He(7-6) transition remain blended with the H(7-6) line at the *Spitzer* spectral resolution. We have used the photoionization code CLOUDY to predict the intensities of the He(7-6) lines relative to the H(7-6) line. This has incorporated the physics described in Porter et al. (2005). The estimate is made using a T_e of 8500 K and N_e of 1000 cm^{-3} consistent with those used in this paper and case B recombination theory. The strongest He(7-6) component is the combined triplet and singlet multiplet $7i \ ^3I \rightarrow 6h \ ^3H^o$ and $7i \ ^1I \rightarrow 6h \ ^1H^o$ at $12.366519 \mu\text{m}$. Next strongest is the combined triplet and singlet multiplet $7h \ ^3H^o \rightarrow 6g \ ^3G$ and $7h \ ^1H^o \rightarrow 6g \ ^1G$ at $12.3657 \mu\text{m}$. This is followed by the combined triplet and singlet multiplet $7g \ ^3G \rightarrow 6f \ ^3F^o$ and $7g \ ^1G \rightarrow 6f \ ^1F^o$ at $12.3618 \mu\text{m}$. Other multiplets that would also blend are weaker and not used for this estimate. If the appropriate He^+/H^+ value were 0.085 at the location of our chex, then summing the above transitions for He(7-6) would result in an expected flux ratio $\text{He}(7-6)/\text{H}(7-6) = 0.065$. In terms of the contribution of the He(7-6) components to the *entire* observed blend [H(7-6) + H(11-8) + He(7-6)], it would be 0.055. However, it is very unlikely that at our chex locations SE of the Bright Bar, that He^+/H^+ is that large. Because we are unable to estimate how much smaller the ratio might be, we do

not apply any correction to values for Ne/H and S/H derived herein. We may safely conclude that any upward adjustment to these metallicities would be *no larger than a factor of 1.055* and likely only a few percent. We note that all three He(7-6) components are on the blue side of H(7-6) while H(11-8) is on the red side. At the limited *Spitzer* spectral resolution, we see no systematic velocity shift or increase in the H(7-6) FWHM with respect to the other lines measured in Table 2.

Figure 12 shows the Ne/H values. These are the sum of the Ne^+/H^+ and $\text{Ne}^{++}/\text{H}^+$ ratios listed in Table 10 along with the propagated uncertainties. There appears to be little variation with position for all chex. The H(7-6) line was not detected at V3, thus there are only lower limits at this outermost position. Following the same method as for the Ne/S ratio, utilizing just the innermost 8 chex, the median value $\text{Ne}/\text{H} = 1.01 \times 10^{-4}$; the sample mean and variance yields $(0.99 \pm 0.07) \times 10^{-4}$. If we also include the 6 independent measurements at V1 and V2, the median becomes $\text{Ne}/\text{H} = 1.03 \times 10^{-4}$, while the sample of 14 mean and variance is $(1.01 \pm 0.08) \times 10^{-4}$. In terms of the conventional expression, this is $12 + \log(\text{Ne}/\text{H}) = 8.00 \pm 0.03$.

Figure 13 shows the S/H estimates from the *Spitzer* data. These are the sum of the S^{++}/H^+ and S^{3+}/H^+ ratios in Table 10 along with the propagated uncertainties. There appears to be little variation with position until reaching the V2 position. Once again we use the mean for the innermost 8 chex as the best value $\text{S}/\text{H} = 6.58 \times 10^{-6}$. The drop in the estimated S/H as indicated by all three independent measurements at V2 is likely due to the onset of more sulfur being tied up in grains. For these 8 innermost chex, we again make a correction for S^+ , unseen by *Spitzer*, by using the S^+/S^{++} ratios derived from the optical data here. The best *corrected* $\text{S}/\text{H} = (7.68 \pm 0.30) \times 10^{-6}$ or $12 + \log(\text{S}/\text{H}) = 6.89 \pm 0.02$.

Esteban et al. (2004) made deep optical echelle spectra within the inner Huygens Region. They used empirical methods to derive gas-phase elemental abundances. According to their table 14, for collisionally-excited lines (CELs), they range from $12 + \log(\text{Ne}/\text{H}) = 7.78 \pm 0.07$ to 8.05 ± 0.07 ($\text{Ne}/\text{H} = 6.03 \times 10^{-5}$ to 1.12×10^{-4}) depending on various ionization correction factors and whether they assume no T_e variations or a mean-square T_e variation factor, t^2 (Peimbert 1967) of 0.022, respectively. Similarly for sulfur, they found $12 + \log(\text{S}/\text{H}) = 7.06 \pm 0.04$ to 7.22 ± 0.04 ($\text{S}/\text{H} = 1.15 \times 10^{-5}$ to 1.66×10^{-5}).

5.3. Fe/H

The discussion in section 4.2.3 is very relevant to our derivation of the Fe/H abundances. Figure 14 plots the Fe/H estimates from the *Spitzer* data. These are the sum of the Fe^+/H^+

and $\text{Fe}^{++}/\text{H}^+$ ratios in Table 10 along with the propagated uncertainties. There appears to be little variation with position except for the V3 position. We stress that the Fe^+/H^+ ratios are derived from the $[\text{Fe II}] 26 \mu\text{m}$ line, which as discussed no doubt has an unknown significant PDR contribution. Because of this, the Fe^+/H^+ ratios are overestimated, causing the Fe/H estimates for chex I4 – V2 in Figure 14 to be deemed an *upper limit*. While the surface brightness of the $[\text{Fe II}] 26 \mu\text{m}$ line is somewhat smaller at V3 compared with V2, the derived Fe^+/H^+ ratios are much higher because the H(7-6) line is not detected at V3. The three separate V3 points are plotted as lower limits because we use the 3σ upper limit for the H(7-6) line. Nevertheless, the same caveat applies here too, that is, we have not accounted for any PDR contribution to the $26 \mu\text{m}$ line. Hence, it is incorrect to conclude that the gas-phase Fe/H abundance at V3 is as high as these 3 points indicate. Subject to all the uncertainty, we follow the same method of using the median for the innermost 8 chex to estimate an upper limit for the gas-phase $(\text{Fe}^+ + \text{Fe}^{++})/\text{H}^+ = 1.39 \times 10^{-6}$. However, Fe^{3+} has not been accounted for and that would necessitate an *increase* in the estimate above for an assessment of the *total gas-phase Fe/H*.

Indeed, there is little that can be contributed in this paper to the determination of the total or even the gas-phase Fe/H abundance. As mentioned in section 4.2.3, there is the uncertainty of how much Fe^{3+} there might be, which could be particularly important for the inner chex positions. Furthermore there have been a number of studies that conclude iron must be substantially tied up in dust grains even within the H II region (e.g., Rodríguez 2002 and references therein).

From their deep optical echelle spectra within the inner Huygens Region, Esteban et al. (2004) used empirical methods to also derive the gas-phase Fe/H abundance ratio. According to their table 14, they range from $12 + \log(\text{Fe}/\text{H}) = 5.86 \pm 0.10$ to 6.23 ± 0.08 ($\text{Fe}/\text{H} = 7.24 \times 10^{-7}$ to 1.70×10^{-6}) depending on various ionization correction factors and whether they assume no T_e variations or a mean-square T_e variation factor, t^2 (Peimbert 1967) of 0.022, respectively.

6. Characterization of the Bright Bar and Outer Veil as an H II region – PDR interface

While *Spitzer* is an admirable machine for measuring both Ne and S abundances in H II regions, the neon abundances are determined more reliably. As previously mentioned, this is because with *Spitzer* observations alone, we are neither accounting for S^+ nor S that may be tied up in dust. Thus it is preferable here to ratio silicon (and other heavy elements) to neon because neon is so well determined with both the 12.8 and $15.6 \mu\text{m}$ lines well measured

all the way to the extended Orion outer boundary at V3. We list the $\text{Si}^+(\text{Ne}^+ + \text{Ne}^{++})$ ratio in Table 10 and show it versus D in Figure 15. Our derivation of the Si^+ abundance assumes that *all* the [Si II] 34.8 μm line emission arises within the ionized region and does not include the very significant PDR contribution at much lower characteristic temperatures (e.g., Kaufman et al. 2006). This caveat is similar to what was discussed for the [Fe II] 26 μm line (see section 4.2.3). Thus, the Si^+/Ne values here must be considered *upper limits*. Figure 15 shows at first a monotonic decrease in this ratio moving outward from the Bright Bar from I4 to M1 ($D = 2.6 - 5.1'$). The ratio then increases with distance from V1 to V3 ($D = 8.8 - 12.1'$) with excellent repeatability amongst the 3 independent observations. There is a dramatic increase at V3.

It is well established that the [Si II] 34.8 μm line in Orion predominantly arises in the PDR but also is produced in the ionized region (Rubin, Dufour & Walter 1993). It is possible that the drop in the estimated Si^+/Ne ratio from I4 to M1 ($D = 2.6 - 5.1'$) is due to a residual influence of the Bright Bar contributing significantly to F(34.8), although this is a stretch for I1 and M1 given that they are far from the BB. Nevertheless, there is a robust conclusion that we may draw here; that the dramatic rise at V3 must be due to a very substantial PDR 34.8 μm contribution. This is a strong piece of evidence that V3 is viewing an H II region – PDR interface. This picture is consistent with many of the other Figures indicating a large change at V3. In a manner similar to Figure 15, we also have plotted the $(\text{Fe}^+ + \text{Fe}^{++})/(\text{Ne}^+ + \text{Ne}^{++})$ ratio versus D (not included in this paper). This shows a giant leap up at V3 even when we take Fe^{++} as zero (recall it was not detected at V3). We attribute this rise due to a very substantial PDR 26.0 μm contribution.

The set of measured hydrogen lines may also prove particularly useful to disentangle emission arising in the ionized H II region and the PDR. Figure 16 displays in four panels the flux ratio versus D of the H(7–6) line, which arises in the H II region, along with the three H_2 lines – H_2 S(2) 12.28, H_2 S(1) 17.04, and H_2 S(0) 28.22 μm – which arise in the PDR. Here we discuss panel (a) only – the flux ratio of the adjacent lines H(7–6) 12.4/ H_2 S(2) 12.3. The intensity of the H(7–6) line falls monotonically with increasing D, except for an increase at V2 compared with V1. For all three observations at V3, H(7–6) was not detected (see the upper limits in Table 2), which indicate that it is faintest by far at V3. The H(7–6)/ H_2 S(2) flux ratio shows an increase at I1, M2, and M3 compared to adjacent chex. This is somewhat reminiscent of the behaviour of the F(22.9)/F(26.0) ratio (see Fig. 10), where we raised the possibility that the lower F(22.9)/F(26.0) ratios at I4, I3 and I2 might be due to some residual influence of the Bright Bar contributing significant PDR F(26.0) emission. In the case of Figure 16 (a), the H(7–6)/ H_2 S(2) flux ratio would be lower because of the Bright Bar PDR still enhancing the H_2 lines. However, the ratio at M1 does not fit the pattern. More definitively, the upper limit to the flux ratio at V3 does comport with

the other evidence that there is a very substantial PDR line contribution at V3. Indeed the $\text{H}_2 \text{S}(2)$ and $\text{H}_2 \text{S}(1)$ lines have become brighter with increasing D from V1 to V3, and at V3 are brighter than at I1 and almost as bright as at M1 (see Table 2). This is yet another strong piece of evidence that V3 is indeed sampling an H II region – PDR interface. While it is beyond the scope of this paper, we do note that this set of *Spitzer* data should provide a means to compare, test, and interpret with a detailed photoionization modeling effort that treats both the H II region and the PDR.

7. Discussion

After a 2009 conference talk on the subject of this paper, one of the leading experts on PDR modeling, and the Orion Nebula Bright Bar (BB) specifically, told RR that he/she was surprised to hear that there were lines of high-ionization species beyond (SE of) the BB. This individual thought that the BB quenched all ionizing radiation. After all, there is a definite transition from the ionized H II region to the PDR at the BB – per the famous 3-colour image of the PDR by Tielens et al. (1993) mentioned earlier. We posit that the reconciliation of that view with the observations/analysis/results here supplies important information regarding the BB. As generally believed, the BB may be treated as a \sim plane-parallel slab, viewed nearly edge-on to the line of sight. This slab is at much higher density than the adjacent material within the H II region (NW of the BB, that is, the side closer to θ^1 Ori C). The amount of matter at these higher densities within the slab is sufficient to soak up all the ionizing (≥ 13.6 eV) photons, causing the PDR. Our *Spitzer* results demand a scenario in which copious ionizing photons penetrate to **much larger distances** SE of the BB. A simple and reasonable explanation is that the slab representing the BB is a *localized escarpment* within the confines of the larger Orion Nebula picture.

In this picture, the BB slab will quench the ionizing photons emanating from θ^1 Ori C over a very limited solid angle. There will then be foreground and background emission along sight lines to the BB that is not produced in the BB. Because of the high density within the slab, the contribution to the emission measure through the (edge-on) length of the BB will be by far the majority of the emission measure integrated over the entire line-of-sight column. Hence this foreground and background emission, including spectral lines of higher-ionization species, not generated within the BB will be dwarfed by the emission produced within the BB. Once the line of sight is clear of the dominating influence of the BB, the character of this harder spectrum can be seen SE of the bar. It would be expected that the BB will create a shadow-zone volume that is devoid of direct ionizing photons from θ^1 Ori C, but again over a limited solid angle. There is the possibility that the BB is clumpy and/or has holes,

allowing radiation to penetrate to the ‘shadowed’ side. However this appears to be ruled out by the observations and modeling of the BB (Tauber et al. 1994; Tielens et al. 1993).

There was previous IR evidence of species as high ionization as O^{++} beyond the BB from *KAO* observations (Simpson et al. 1986). Without question, there is abundant evidence from optical observations beyond the BB of line emission from O^{++} , as well as other ionic species found in H II regions. Indeed, one need look no further than the optical spectra presented here in Tables 4–7. Even at the most distant position V3, lines are measured from the following higher-ionization species (along with the ionization potential to create the ion): He I (24.6 eV), [Ar III] (27.6 eV), [O III] (35.1 eV), and [Ne III] (41.0 eV). The problem with interpreting these optical observations is due to the fact that much of the emission may be photons scattered from the much brighter inner Huygens Region (O’Dell 2001; O’Dell & Goss 2009). Because scattering is wavelength dependent, it is unknown how much of the observed optical line emission is produced in situ and how much is the scattered component.

The mid-IR *Spitzer* lines suffer far less from scattering than do the optical lines, providing another inherent advantage when interpreting them in terms of nebular properties, including abundances. As mentioned in §4.2, the other advantages, compared with the optical, are that they are far less sensitive to T_e and fluctuations in T_e (t^2) and suffer far less from extinction. Because of these important advantages, together with the ability of *Spitzer* to measure all the pertinent neon species along with the H(7–6) line in the same spectra, and the fact that Ne will not be incorporated in grains and molecules, the Orion Nebula $Ne/H = (1.01 \pm 0.08) \times 10^{-4}$ ($12 + \log (Ne/H) = 8.00 \pm 0.03$) is one of the most robust determinations of *total* metallicity for any element in any H II region. It is somewhat ironic that while Ne/H is the poorest determined amongst the most abundant elements in the Sun, it is (arguably) the best determined heavy element abundance ratio in Orion – a worthy benchmark standard.

There have been more estimates of the gas-phase Ne/S abundance ratio using *Spitzer* data than Ne/H due to the weakness of the H(7–6) line relative the Ne and S lines used. We reviewed the situation with regard to Ne/S in R08 (see figures 11 and 12 in that paper). The value we determine here 13.0 ± 0.6 is in reasonable accord with those found in R08 for the higher ionization regions. However, all of the results in R08 used a different effective collision strength for [Ne II] as discussed earlier. Our transition to using Griffin et al. (2001) instead of Saraph & Tully (1994) values will result in a downward revision to Ne/S in the R08 estimates by as much as 10 per cent for the lower ionization H II regions, but a smaller change for those at higher ionization. We defer a reanalysis of the results in R08 to a later paper in which we will also present our *Spitzer* observations of a number of H II regions in the dwarf irregular galaxy NGC 6822.

8. Summary and conclusions

We obtained *Spitzer* IRS observations at 11 positions in the Orion Nebula all southeast of the Bright Bar and extending in a straight line to more than 12' from the exciting star θ^1 Ori C. These spectra were taken with both the short-high (SH) and long-high (LH) modules using an aperture grid patterns chosen to very closely match the same area in the nebula. In addition, we have made new ground-based, long-slit spectra that correspond closely with the 11 regions observed with *Spitzer*. Orion is the benchmark for studies of the interstellar medium, particularly for elemental abundances. With these data, we focus predominantly on neon, the fifth most abundant element in the Universe, and sulfur, one of the top ten, because of the specific capability that *Spitzer* provided. Our major points are enumerated below.

(1) The Ne/H abundance ratio is especially well determined, with a value of $(1.01 \pm 0.08) \times 10^{-4}$. In terms of the conventional expression, this is $12 + \log(\text{Ne}/\text{H}) = 8.00 \pm 0.03$. This may well be the *gold standard* for a determination of metallicity in an H II region.

(2) We estimate the Ne/S gas-phase abundance ratio by observing the dominant ionization states of Ne (Ne^+ , Ne^{++}) and S (S^{++} , S^{3+}) with *Spitzer*. The optical data are used to correct our *Spitzer*-derived Ne/S ratio for S^+ , which is not observed with *Spitzer*. Excluding all three outermost ‘Veil’ positions, we find the median value adjusted for the optical S^+/S^{++} ratio is $\text{Ne}/\text{S} = 12.8$. From the internal scatter amongst these 8 values, we obtain a sample mean and variance of 13.01 ± 0.64 .

(3) A dramatic find is the presence of species as high-ionization as Ne^{++} all the way to the outer optical boundary $\sim 12'$ from θ^1 Ori C. At these locations beyond the Bright Bar, where the transition from ionized to photo-dissociation region lines is purported to be complete, it was somewhat surprising to find the high ionization lines of [S IV] 10.51 and [Ne III] 15.56 μm present with excellent signal-to-noise (S/N) ratios. A likely possibility is that the Bright Bar is an escarpment that is quenching the ionizing radiation from θ^1 Ori C over a *localized solid angle*. As usually characterized, the Bright Bar is seen nearly edge-on. The depth along the line of sight is not known. Thus there can be copious ionizing radiation in the foreground (and the background) that does not encounter the Bar at all. Such a scenario very much modifies a common viewpoint of the Nebula in the SE quadrant. This picture of the ionized H II region continuing SE of the Bar is further supported by our long-slit spectra that sample all the chex. From these we infer T_e values at least as high as 8300 K from the familiar diagnostic line intensity ratios, [N II] 6584/5755 Å and [O III] 5007/4363 Å – values that are typical for the ionized H II region, not PDRs. Likewise, our estimate for the fractional ionic abundance for S^+ is significantly smaller than that for S^{++} .

This IR result is robust, whereas the optical evidence from observation of high-ionization (e.g. O^{++}) at the outer optical boundary suffers uncertainty because of the possible scattering of emission from the much brighter inner Huygens Region. The *Spitzer* spectra are consistent with the Bright Bar being a high-density ‘**localized escarpment**’ in the larger Orion Nebula picture. Hard ionizing photons reach most solid angles well SE of the Bright Bar.

(4) The *Spitzer* data provide an excellent diagnostic of electron density in the S^{++} region from the line flux ratio [S III] 18.7/33.5 μm . Likewise, the ground-based observations provide an excellent diagnostic of N_e in the S^+ region from the line flux ratio [S II] 6716/6731 \AA . From these, we derive the electron density versus distance from θ^1 Ori C (see Figure 7). These two N_e distributions provide a unique perspective for the extended outer Orion Nebula, with the values for N_e [S II] $<$ N_e [S III] at a given distance except for the outermost region V3. The fact that N_e [S II] is lower than N_e [S III] for the most part is expected, as explained in §4.1, where reasons for the behaviour in the outermost region are also offered.

(5) The *Spitzer* data provide substantial evidence that at chex V3, the observations are sampling an H II region – PDR interface. This should not be unexpected since visually this appears to be the outer boundary of the Orion Nebula in this direction. As mentioned in the introduction, it is also the position of the “Veil” seen in projection (essentially edge-on) along our observed radial from θ^1 Ori C. As described in O’Dell (2001), early evidence for this foreground “Veil” stemmed from H I 21-cm line absorption line observations (van der Werf & Goss 1989). The Veil is seen in projection as the outer boundary of M42, the grayish colour extending from roughly north counter clockwise to the southeast (see Figure 5). In a very recent paper (O’Dell & Harris 2010), the case is made that the more likely picture is the following. Instead of the foreground Veil curving back away from the observer to be seen edge-on near V3, it is the background H II region – PDR boundary that is curving up toward the observer. In this view, they suggest the word “Rim” to define this feature. As such, our position V3 is then sampling the “Rim wall” in this particular radial direction from θ^1 Ori C. This difference in perception and nomenclature does not alter the conclusions of the present paper. The following *Spitzer* data support the inference that at V3, we are indeed sampling an H II region – PDR interface.

From the plot of the Si^+/Ne versus D (Figure 15), derived using the [Si II] 34.8 μm line, there is a dramatic increase in this ratio at the outermost V3 position. As detailed in §6, our estimate of Si^+/Ne assumes *all* of the 34.8 μm emission arises in the ionized region and does not account for an unknown PDR contribution. The large increase at the outermost V3 position is strong evidence that the bulk of the [Si II] 34.8 emission arises in a PDR at this H II region – PDR boundary. In a manner similar to Figure 15, we also plotted the $(Fe^+ + Fe^{++})/(Ne^+ + Ne^{++})$ ratio versus D (not included in this paper). This shows a giant leap

up at V3 even when we take Fe^{++} as zero (recall it was not detected at V3). We attribute this rise due to a very substantial PDR $26.0 \mu\text{m}$ contribution. For all three observations at V3, H(7–6) was not detected, an indication that by far it is faintest at V3. On the other hand, the H_2 S(2) and H_2 S(1) lines, with an origin only in the PDR, have become brighter with increasing D from V1 – V3 and at V3 are brighter than at I1 and almost as bright as at M1.

This work is based on observations made with the *Spitzer Space Telescope*, which is operated by the Jet Propulsion Laboratory, California Institute of Technology under NASA contract 1407. Support for this work was provided by NASA for this *Spitzer* programme identification 50082. In addition to the *Spitzer* support, CRO was supported in part by *HST* grant AR 10967. GJF gratefully acknowledges support by NSF (0607028 and 0908877) and NASA (07-ATFP07-0124). We thank Don Clayton and Stan Woosley for providing information on the Ne/S ratio from a nucleosynthesis, galactic chemical evolution perspective. We are grateful for the help of our students – David Ng, Tim Craven, Savannah Lodge-Scharff, Evan Gitterman, Chris Lo, and Atish Agarwala – with various stages of this work. We thank the referee for valuable comments.

REFERENCES

- Abel N.P., Brogan C.L., Ferland G.J., O’Dell C.R., Shaw G., Troland T.H., 2004, *ApJ*, 609, 247
- Abel N.P., Ferland G.J., O’Dell C.R., Shaw G., Troland T.H., 2006, *ApJ*, 644, 344
- Asplund M., Grevesse N., Sauval A.J., Scott P., 2009, *ARA&A*, 47, 481
- Bahcall J.N., Serenelli A.M., Basu S., 2006, *ApJS*, 165, 400
- Baldwin J. A., Ferland G. J., Martin P. G., Corbin M. R., Cota S. A., Peterson B. M., Slettebak A., 1991, *ApJ*, 374, 580
- Baldwin J.A., Verner E.M., Verner D.A., Ferland G.J., Martin P.G., Korista K.T., Rubin R.H., 2000, *ApJS*, 129, 229
- Blagrove K. P. M., Martin P. G., Rubin R. H., Dufour R. J., Baldwin J. A., Hester J. J., Walter D. K., 2007, *ApJ*, 655, 299
- Cami J., Bernard-Salas J., Peeters E., Malek S.E., 2010, *Science* (in press)

- Clayton D.D., 2007, *Science*, 318, 1876
- Drake J.J., Testa P., 2005, *Nature*, 436, 525
- Esteban C., Peimbert M., García-Rojas J., Ruiz M. T., Peimbert A., Rodríguez M., 2004, *MNRAS*, 355, 229
- Froese Fischer C., Tachiev G., Irimia A., 2006, *ADNDT*, 92, 607
- Griffin D. C., Mitnik D. M., Badnell N. R., 2001, *J. Phys. B*, 34, 4401
- Henney W. J., 1994, *ApJ*, 427, 288
- Henney W. J., 1998, *ApJ*, 503, 760
- Henney W. J., O'Dell C. R., Zapata L. A., García-Díaz, Ma. T., Rodríguez, L. F., & Robberto M., 2007, *AJ*, 133, 2192
- Higdon S. J. U., et al., 2004, *PASP*, 116, 975
- Houck J. R., et al., 2004, *ApJS*, 154, 18
- Irimia A., Froese Fischer C., 2005, *Phy. Scripta*, 71, 172
- Jones B. F., Walker M. F., 1988, *AJ*, 95, 1755
- Kaufman M.J., Wolfire M.G., Hollenbach D.J., 2006, *ApJ*, 644, 283
- Lodders K., 2003, *ApJ*, 591, 1220
- Magrini L., Stanghellini L., Villaver E., 2009, *ApJ*, 696, 729
- McLaughlin B.M., Bell K.L., 2000, *J. Phys. B*, 33, 597
- Morel T., Butler K., 2008, *A&A*, 487, 307
- O'Dell C. R., 1998, *AJ*, 116, 1346
- O'Dell C. R., 2001, *ARA&A*, 39, 99
- O'Dell C. R., Goss W. M., 2009, *AJ*, 138, 12350
- O'Dell C. R., Harris J. A., 2010, *AJ* (submitted)
- O'Dell C. R., Walter D. K., Dufour R. J., 1992, *ApJ*, 399, L67

- Osterbrock D. E., Ferland G. J., 2006, *Astrophysics of Gaseous Nebulae and Active Galactic Nuclei* (second edition), University Science Books (Mill Valley)
- Peimbert M., 1967, *ApJ*, 150, 825
- Podobedova L.I., Kelleher D.E., Weise W.L., 2009, *JPCRD*, 38, 171
- Porter R.L., Bauman R.P., Ferland G.J., MacAdam K.B., 2005, *ApJ*, 622, L73
- Pottasch S.R., Bernard-Salas J., 2006, *A&A*, 457, 189
- Ramsbottom A., Bell K. L., Stafford R. P., 1996, *ADNDT*, 63, 57
- Rodríguez M., 2002, *A&A*, 389, 556
- Rodríguez M., Rubin R. H., 2005, *ApJ*, 626, 900
- Rubin R. H., 1989, *ApJS*, 69, 897
- Rubin R. H., Colgan S. W. J., Dufour R. J., Lord S. D., 1998, *ApJ*, 501, L209
- Rubin R. H., Dufour R. J., Ferland G. J., Martin P. G., O’Dell C. R., Baldwin J. A., Hester J. J., Walter D. K., Wen Z., 1997, *ApJ*, 474, 131
- Rubin R. H., Dufour R. J., Walter D. K., 1993, *ApJ*, 413, 242
- Rubin R. H., Martin P. G., Dufour R. J., Ferland G. J., Blagrove K. P. M., Liu X.-W., Nguyen J. F., Baldwin J. A., 2003, *MNRAS*, 340, 362
- Rubin R. H., McNabb I. A., Simpson J. P., Dufour R. J., Pauldrach A. W. A., Colgan S. W. J., Craven T. W., Gitterman E. D., Lo C. C., 2010, *IAU Symp.*, 265, 249 (R10)
- Rubin R. H., Simpson J. P., Colgan S. W. J., Dufour R. J., Brunner G., McNabb I. A., Pauldrach A. W. A., Erickson E. F., Haas M. R., Citron R. I., 2008, *MNRAS*, 387, 45 (R08)
- Rubin R. H., Simpson J. P., Colgan S. W. J., Dufour R. J., Ray K. L., Erickson E. F., Haas M. R., Pauldrach A. W. A., Citron R. I., 2007, *MNRAS*, 377, 1407 (R07)
- Rubin R. H., Simpson J. P., Haas M. R., Erickson E. F., 1991a, *ApJ*, 374, 564
- Rubin R. H., Simpson J. P., Haas M. R., Erickson E. F., 1991b, *PASP*, 103, 834
- Saraph H.E., Tully J.A., 1994, *A&AS*, 107, 29

- Simpson J. P., Colgan S. W. J., Cotera A. S., Erickson E. F., Hollenbach D. J., Kaufman M. J., Rubin R. H., 2007, *ApJ*, 670, 1115
- Simpson J. P., Rubin R. H., Colgan S. W. J., Erickson E. F., Haas M. R., 2004, *ApJ*, 611, 338
- Simpson J.P., Rubin R.H., Erickson E.F., Haas M.R., 1986, *ApJ*, 311, 895
- Smith J. D. T., et al., 2007a, *PASP*, 119, 1133
- Smith J. D. T., et al., 2007b, *CUBISM Handbook*
- Storey P. J., Hummer D. G., 1995, *MNRAS*, 272, 41
- Tauber J.A., Tielens A.G.G.M., Meixner M.M., Goldsmith P.F., 1994, *ApJ*, 422, 136
- Tayal S. S., Gupta G. P., 1999, *ApJ*, 526, 544
- Tenorio-Tagle G., 1979, *A&A*, 71, 59
- Tielens A.G.G.M., Meixner M.M., van der Werf P.P., Bregman J., Tauber J.A., Stutzki J., Rank D., 1993, *Science*, 262, 86
- van der Werf P.P., Goss W.M., 1989, *A&A*, 224, 209
- Wang W., Liu X.-W., 2008, *MNRAS*, 389, L33
- Wen Z., O'Dell C. R., 1995, *ApJ*, 438, 784
- Witthoef M. C., Whiteford, A. D., Badnell N. R., 2007, *J. Phys. B*, 40, 2969
- Woosley S.E., Heger A., 2007, *Phys. Rep.*, 442, 269

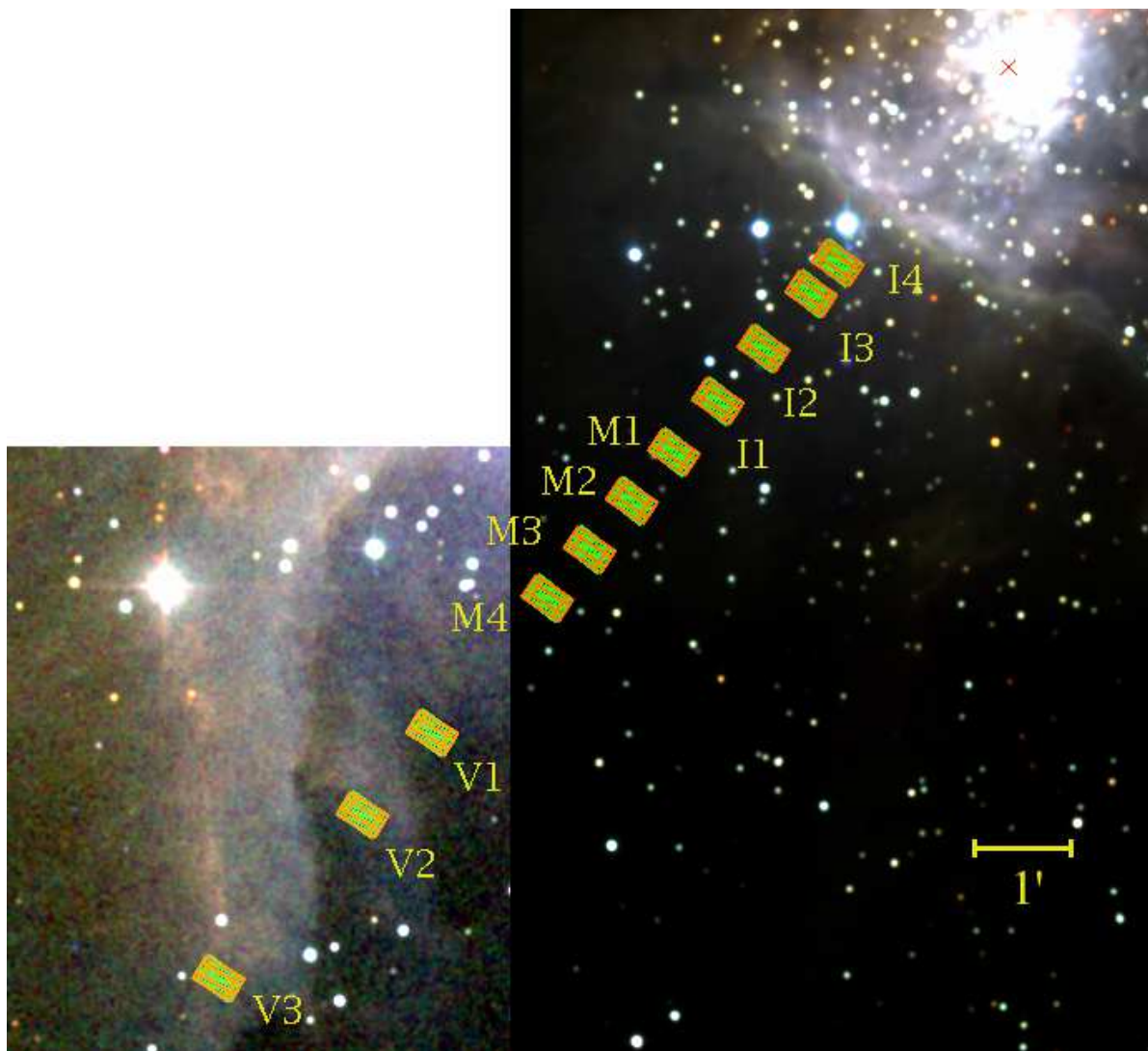


Fig. 1.— This shows our 11 observed *Spitzer* positions for the Orion Nebula (M42, NGC 1976) overlaid on a composite 2MASS image with H- (blue), J- (green), and K-band (red). The aperture mapping (or grid) patterns (that we call “chex”, after the breakfast cereal) for the short high (SH) and long high (LH) modules are shown in green and orange respectively. These are labelled as defined in Table 1. The SH and LH *individual* aperture sizes are respectively $4.7'' \times 11.3''$ and $11.1'' \times 22.3''$ with the orientations roughly orthogonal. The Trapezium is at the top right with the dominant ionizing star θ^1 Ori C marked with a red X. For reference, the star θ^2 Ori A is just N of our NW-most aperture cluster. N is up, E to the left.



Fig. 2.— *Spitzer* short-high (SH) full spectra of all 11 chex. This composite of surface brightness (intensity) versus wavelength has labelled the dominant features. Vertical fiducial lines guide how the features vary with distance from the exciting star θ^1 Ori C.

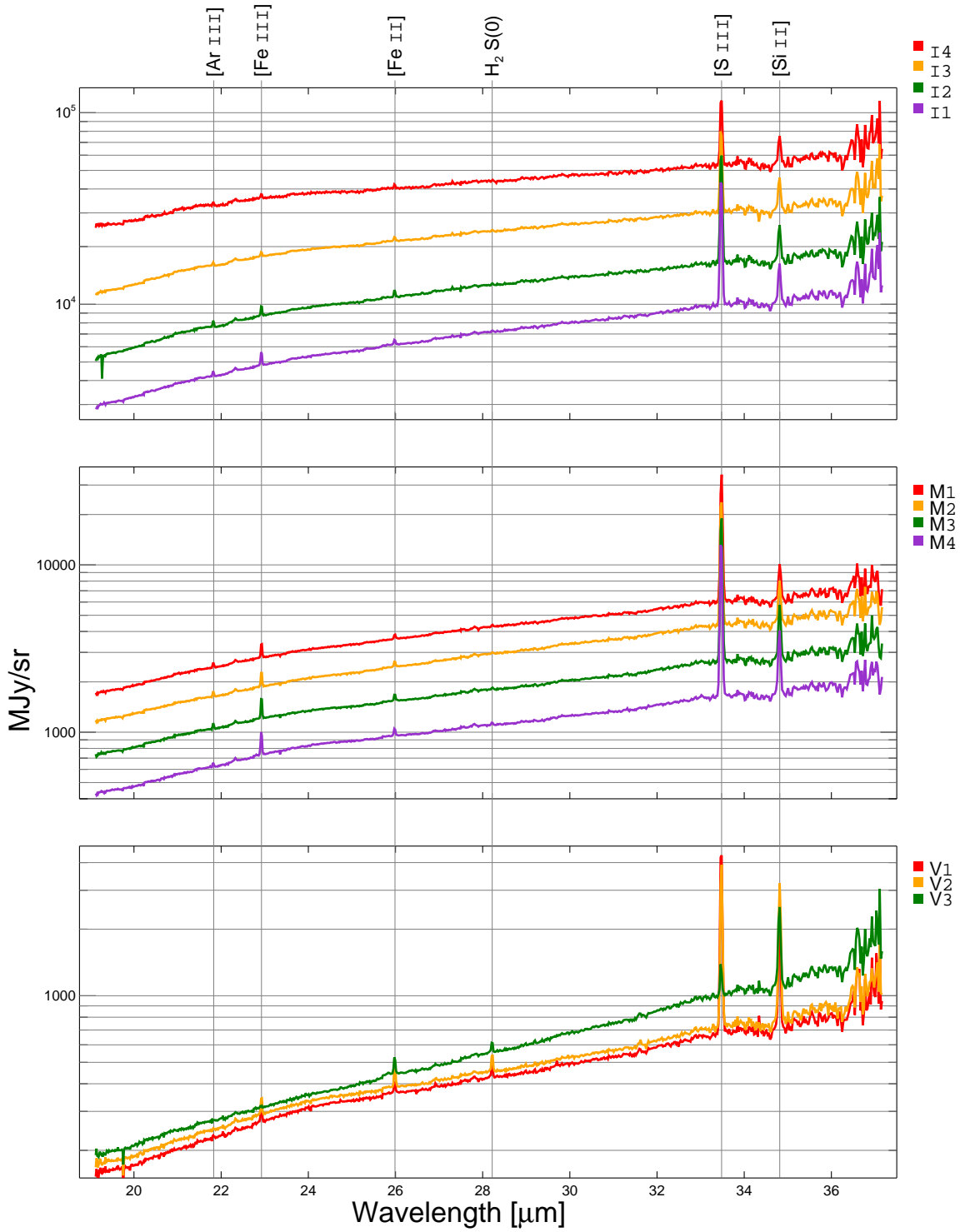


Fig. 3.— The same as Figure 2 for the set of long-high (LH) full spectra of all 11 chex.

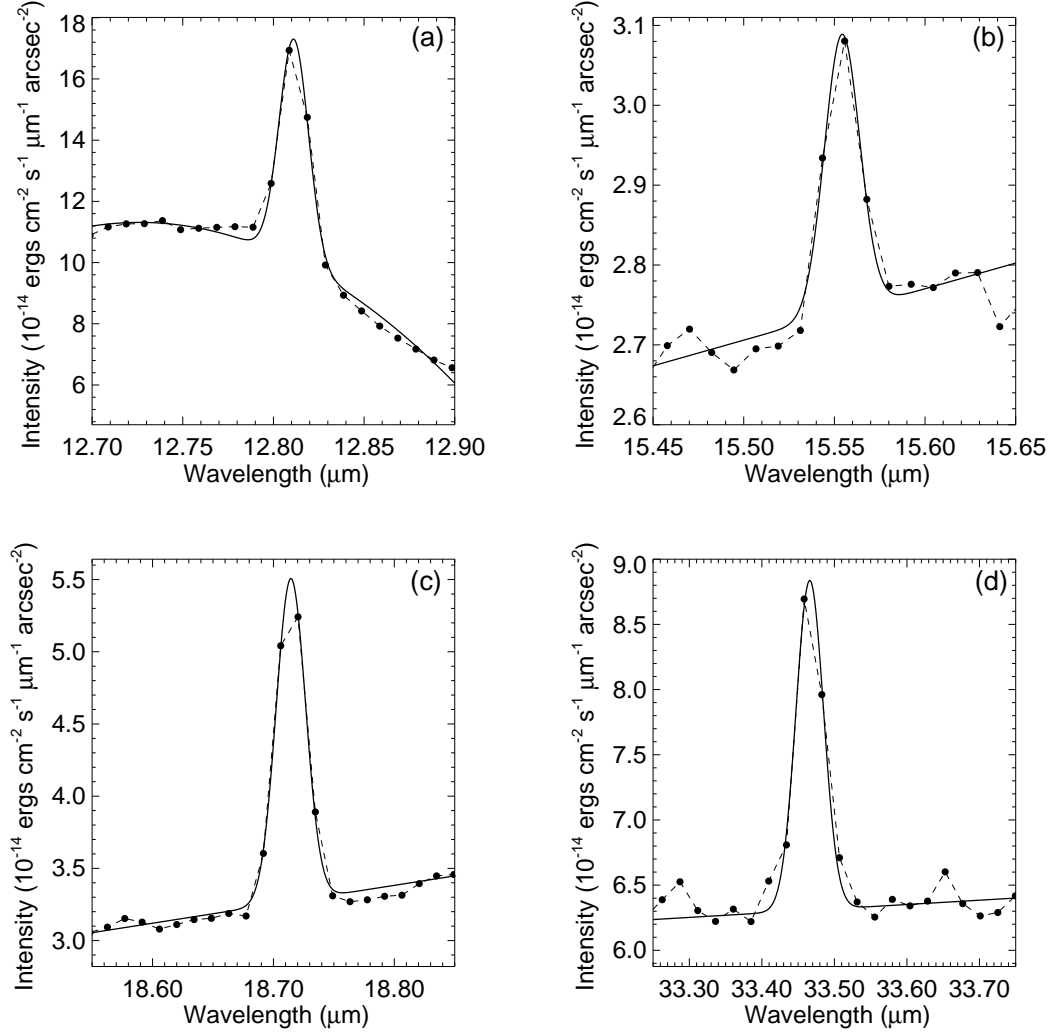


Fig. 4.— Measurements of four emission lines in chex V3, the outermost one (see Fig. 1) and for just one (data set 25380864) of the three AORs where all three of the veil chex were observed: (a) [Ne II] $12.8 \mu\text{m}$; (b) [Ne III] $15.6 \mu\text{m}$; (c) [S III] $18.7 \mu\text{m}$; and (d) [S III] $33.5 \mu\text{m}$. The data points are the filled circles. The fits to the continuum and Gaussian profiles are the solid lines. These are among the lines listed in Table 2 for V3-1, that is chex V3 and veil AOR 1. Such measurements provide the set of line intensities for further analysis.

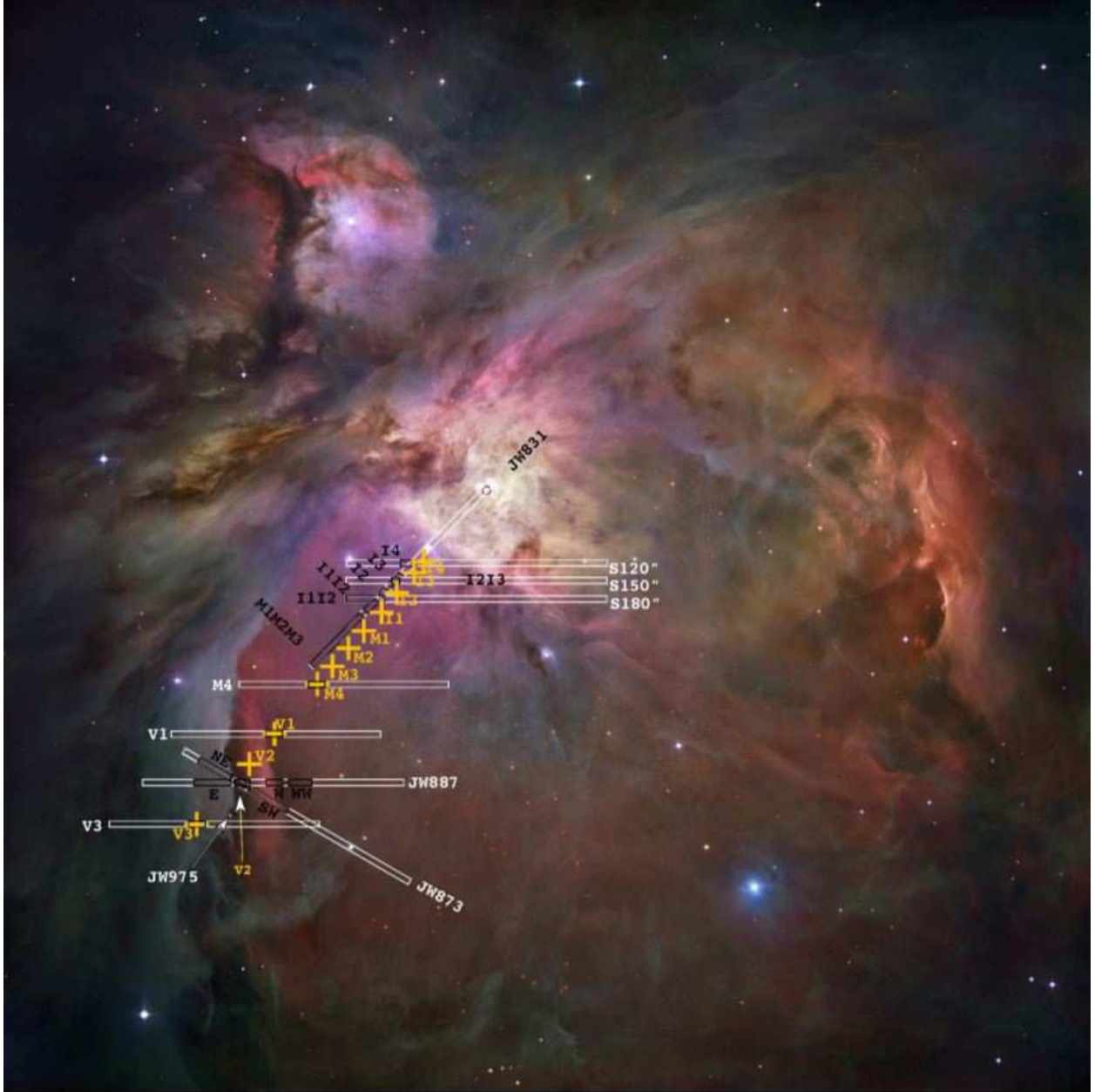


Fig. 5.— This $1200'' \times 1200''$ image of the Orion Nebula taken from Henney et al. (2007) shows the regions sampled in our spectroscopy. The white boxes show the slit positions and are labelled with the reference star used, this being θ^1 Ori C for the east-west slits displaced south of that star, or with the name of the *Spitzer* chex. For clarity the slits are shown as $10''$ wide even though they were actually $2.6''$ wide. The yellow crosses indicate the centre of regions observed with *Spitzer*, while the dark boxes and labels indicate the ground-based optical spectroscopy samples.

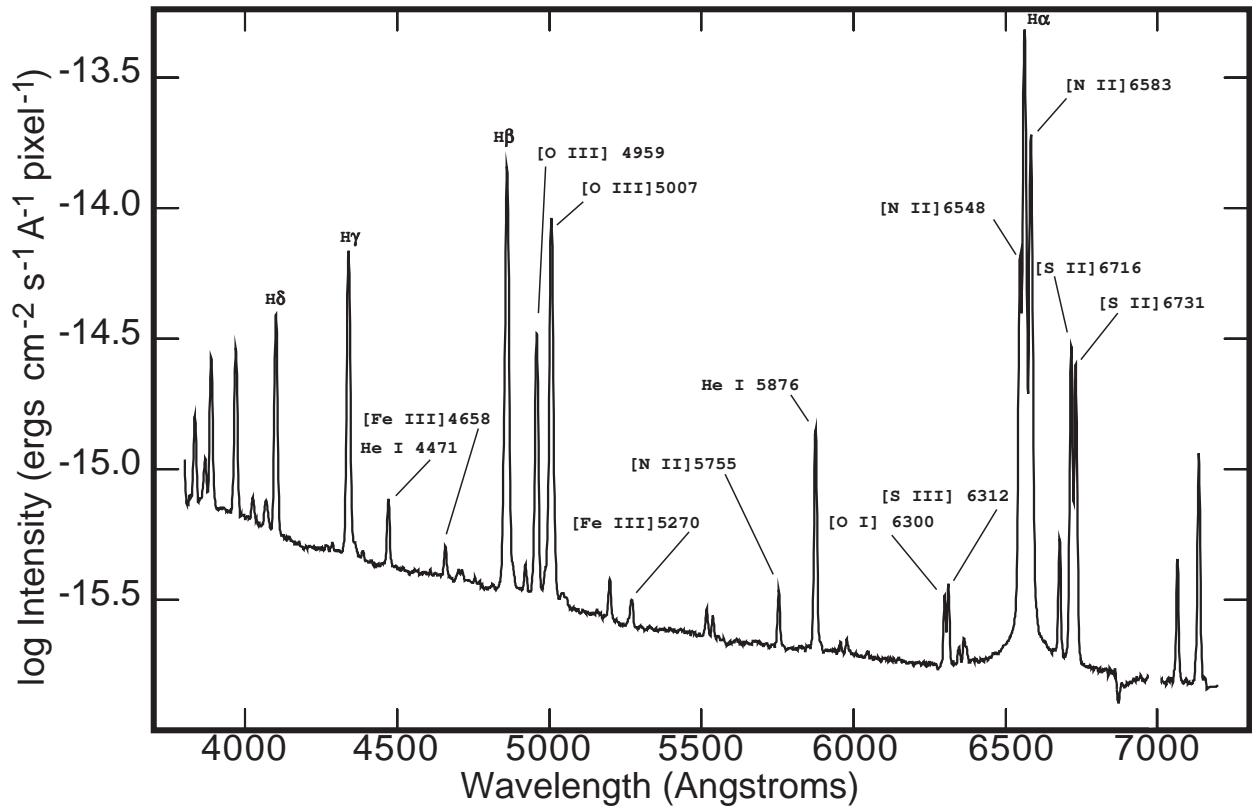


Fig. 6.— This is a logarithmic presentation of a representative optical spectrum. It is the result of 3900 seconds of integration over five exposures of the M4 extraction along 21 pixels of the M4 long slit (see Figure 5). The gap in data near 7000 Å is due to a column defect in the CCD detector.

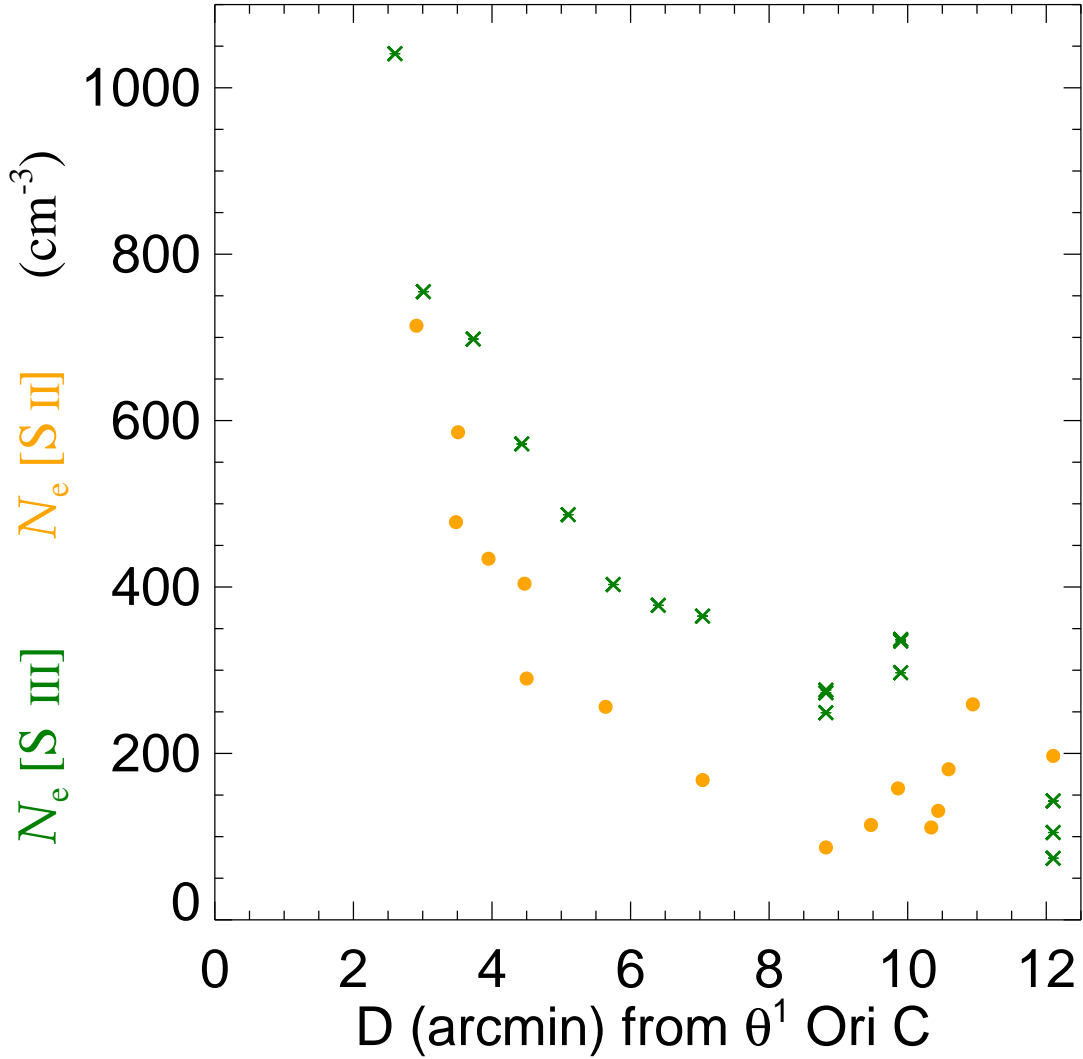


Fig. 7.— Plot of the electron density N_e [S III] (dark or green in colour) x's and N_e [S II] (gray or yellow in colour) circles versus D (the distance in arcmin from θ^1 Ori C to the centre of the *Spitzer* chex or ground-based optical sample).

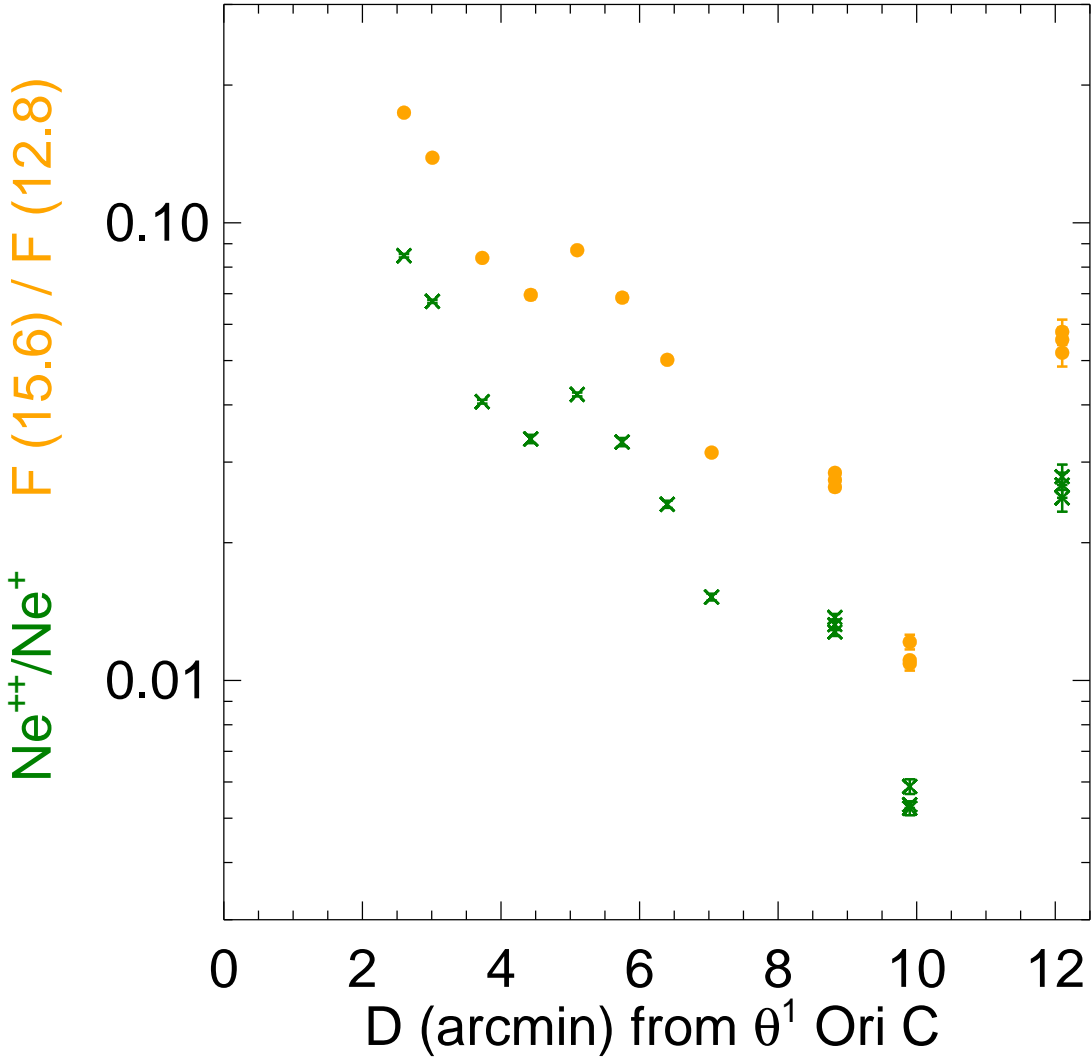


Fig. 8.— Plot of the line flux ratio $[\text{Ne III}] 15.6/[\text{Ne II}] 12.8$ (gray or yellow in colour) and the derived $\text{Ne}^{++}/\text{Ne}^+$ (black or green in colour) versus D . Error bars here and in Figs 9–16 are for the propagated measurement uncertainties and do not include the systematic uncertainties (see text).

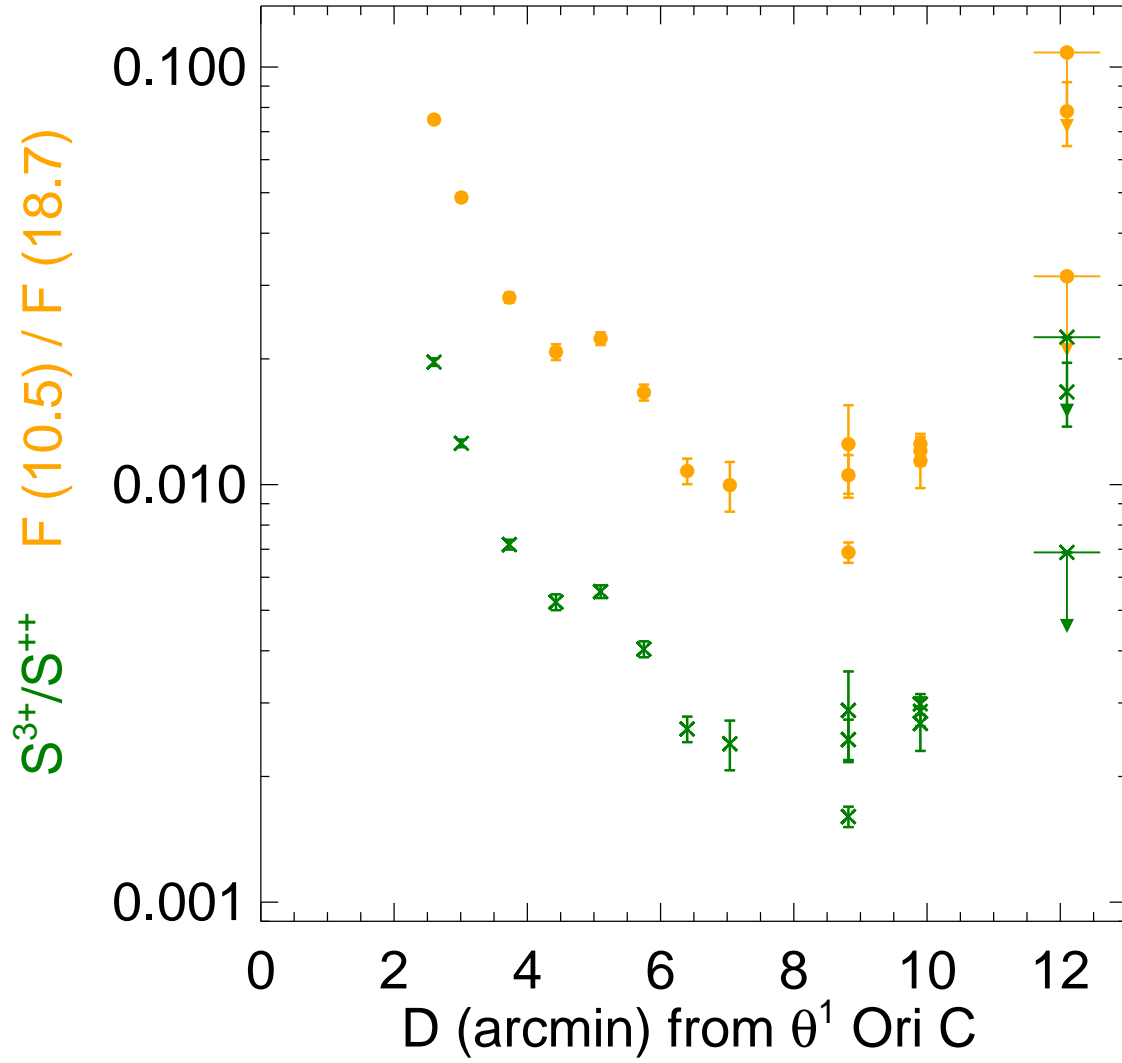


Fig. 9.— Plot of the line flux ratio $[S\text{ IV}] 10.5/[S\text{ III}] 18.7$ (gray or yellow in colour) and the derived S^{3+}/S^{2+} (black or green in colour) versus D .

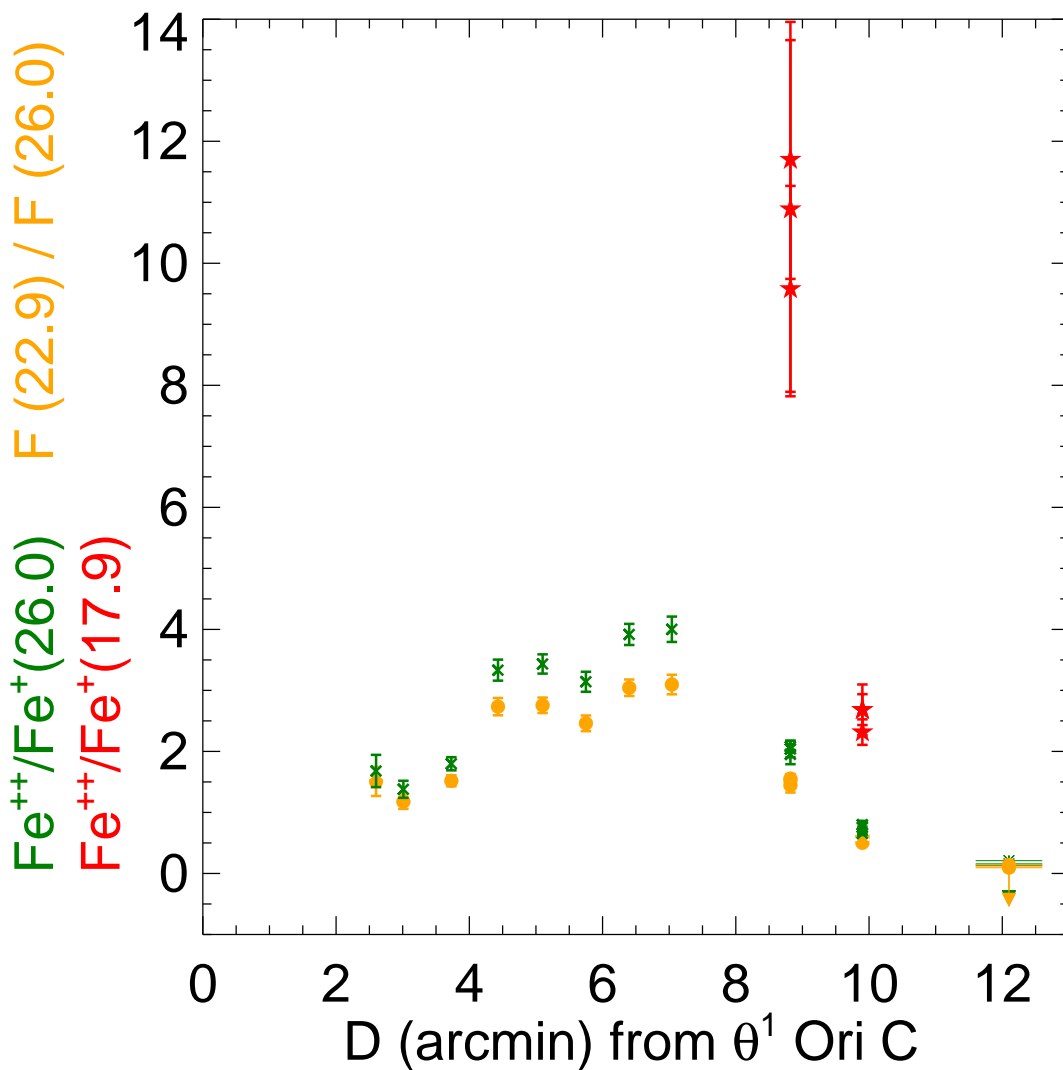


Fig. 10.— Plot of the line flux ratio $[Fe\ III]\ 22.9/[Fe\ II]\ 26.0$ (gray or yellow circles in colour) and the derived Fe^{++}/Fe^{+} (black or green x in colour) versus D . In addition, the $[Fe\ II]\ 17.9\ \mu m$ line was measured at V1 and V2 only. The Fe^{++}/Fe^{+} derived from the $[Fe\ III]\ 22.9/[Fe\ II]\ 17.9$ ratio is shown (black or red stars in colour). These higher values are a more accurate measure of Fe^{++}/Fe^{+} than those using the $[Fe\ II]\ 26.0$ line, which are **lower limits** (see text).

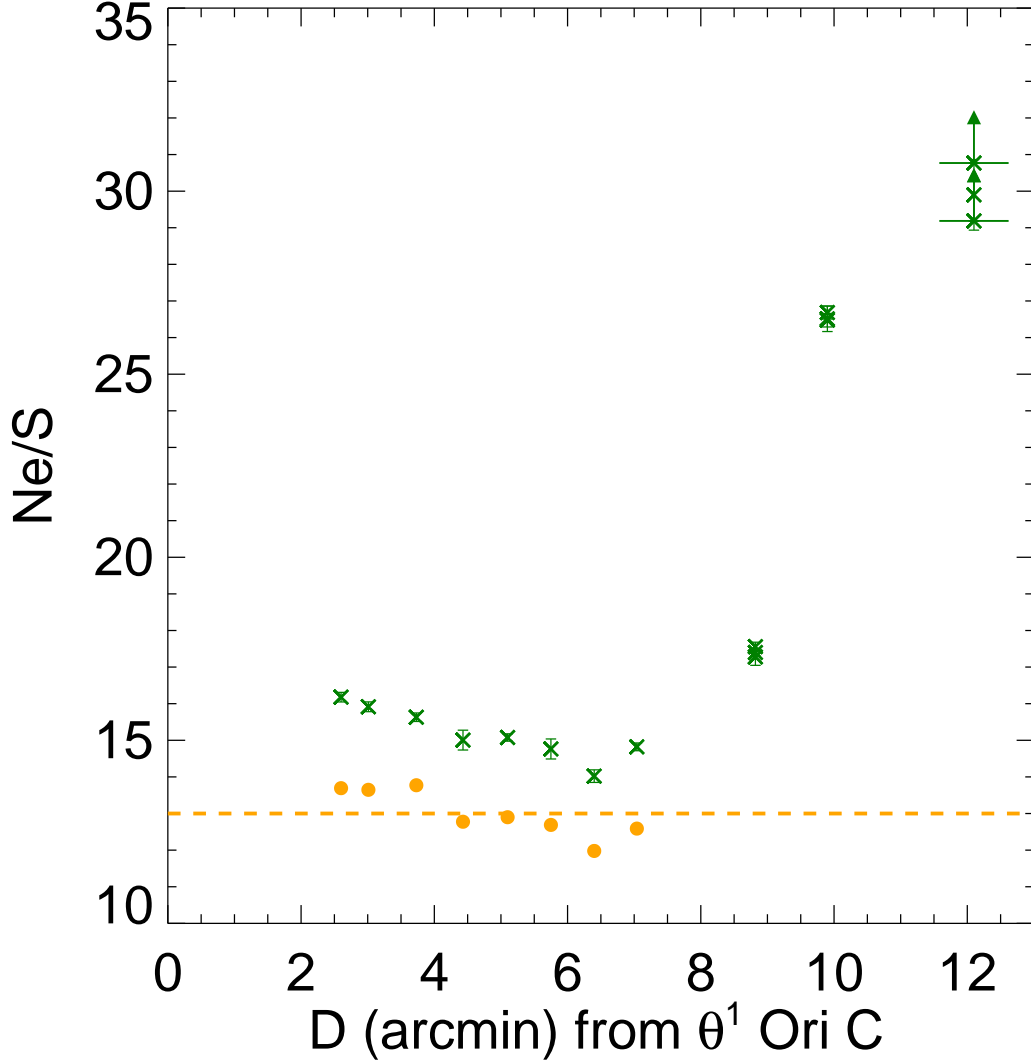


Fig. 11.— Plot of Ne/S versus D. The dark or green x in colour represent the the gas-phase Ne/S ratio as approximated by the $(\text{Ne}^+ + \text{Ne}^{++})/(\text{S}^{++} + \text{S}^{3+})$ ratio derived from the *Spitzer* data only. These should be considered as upper limits to the Ne/S ratio because sulfur in S^+ has not been accounted for. The gray or yellow circles in colour show the $(\text{Ne}^+ + \text{Ne}^{++})/(\text{S}^+ + \text{S}^{++} + \text{S}^{3+})$ ratio after adjusting the *Spitzer*-only data by the optically-determined S^+/S^{++} ratios for the inner 8 chex (see text). The dashed horizontal line is the mean value for these 8 chex and represents our best estimate for the gas-phase $\text{Ne/S} = 13.0 \pm 0.6$.

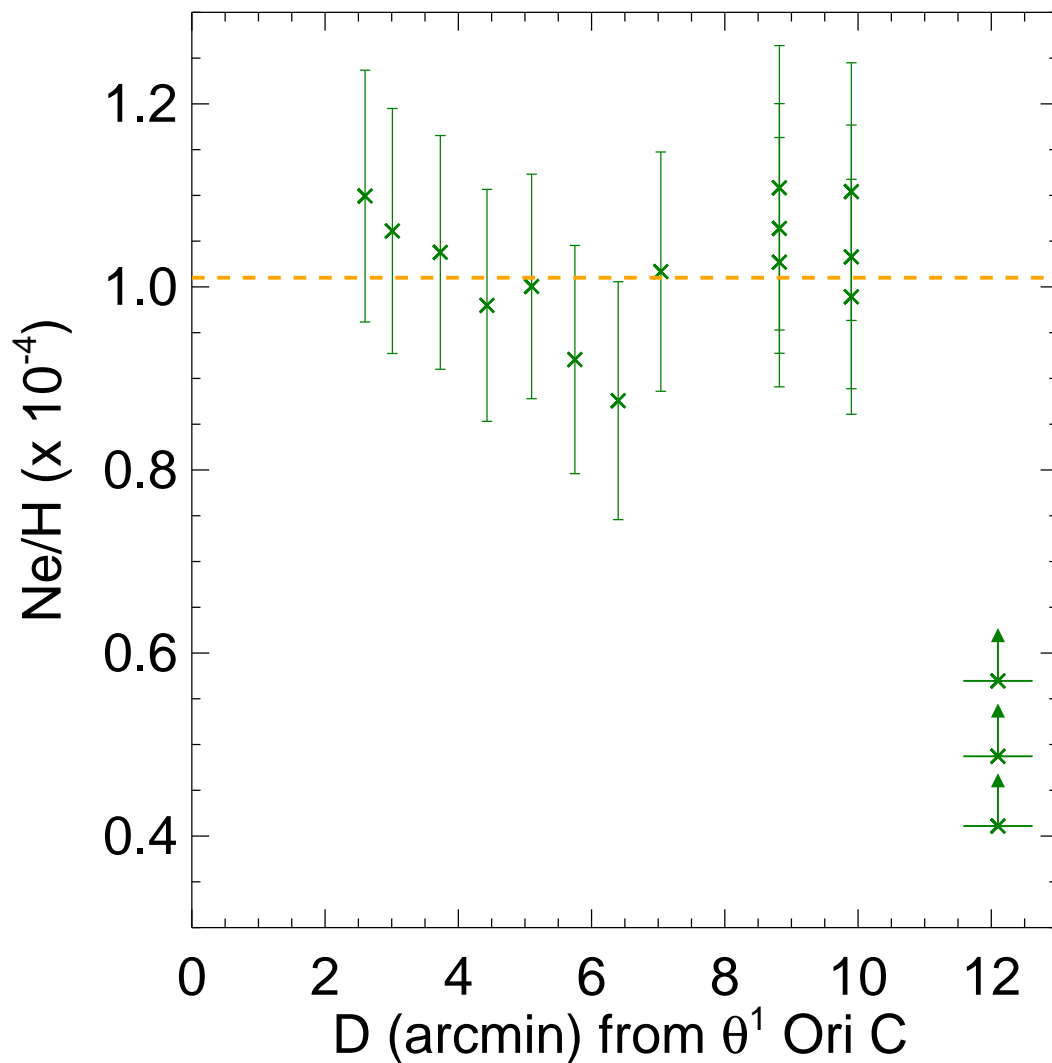


Fig. 12.— Plot of Ne/H versus D. Except for chex V3 where the H(7–6) line was not detected, the ratios vary little. We include the 6 independent measurements at V1 and V2 and take the mean for the 10 innermost chex as the best value, $\text{Ne}/\text{H} = (1.01 \pm 0.08) \times 10^{-4}$. In terms of the conventional expression, this is $12 + \log(\text{Ne}/\text{H}) = 8.00 \pm 0.03$. This may well be the *gold standard* for a determination of metallicity in an H II region (see text)

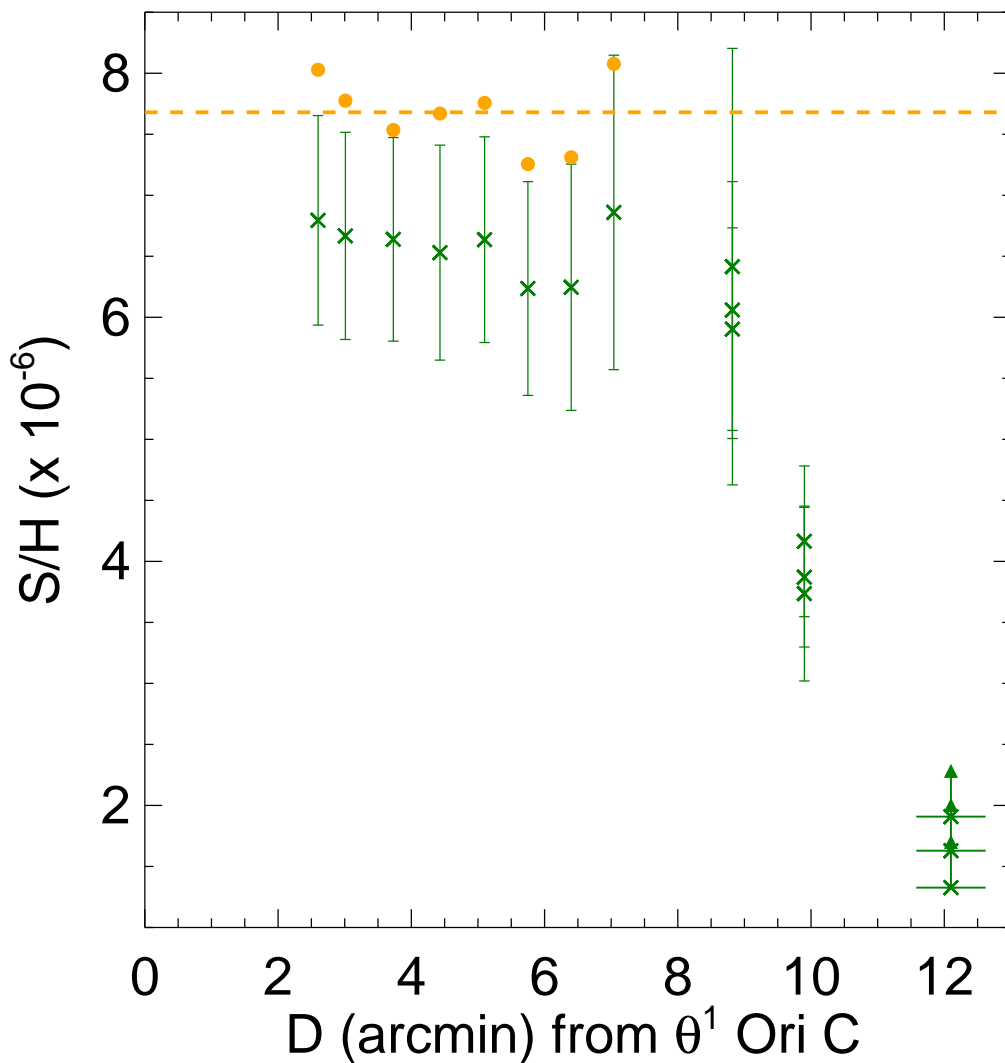


Fig. 13.— This figure shows the S/H estimates versus D . Here we plot the sum of the S^{++}/H^+ and S^{3+}/H^+ ratios using the *Spitzer* data only. As for Ne/S , we use the mean for the innermost 8 chex as the best value $S/H = (6.58 \pm 0.23) \times 10^{-6}$. For these 8 innermost chex, we again make a correction for S^+ , unseen by *Spitzer*, by using the S^+/S^{++} ratios derived from our optical data. These points are the filled circles (yellow in the colour version). The best *corrected* $S/H = (7.68 \pm 0.30) \times 10^{-6}$ or $12 + \log(S/H) = 6.89 \pm 0.02$.

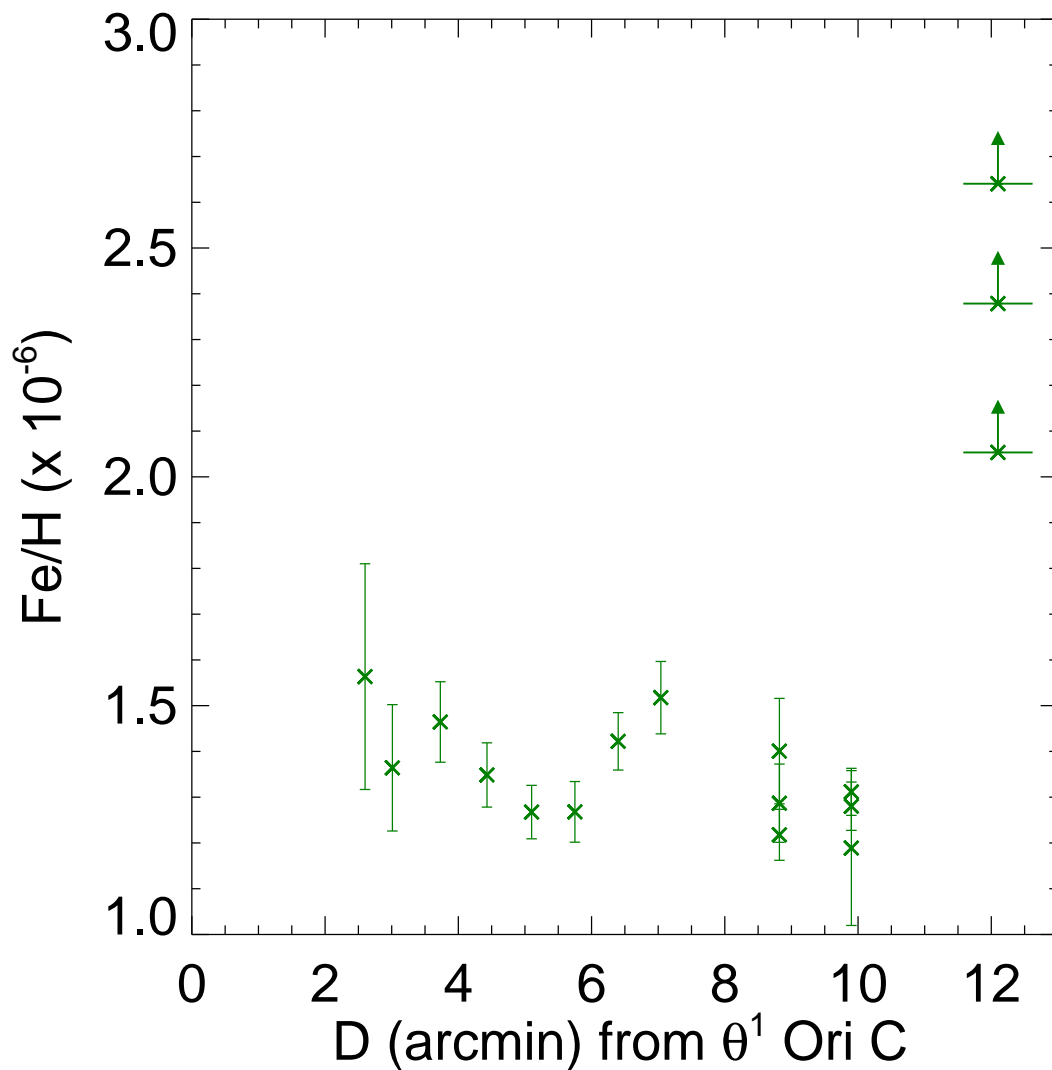


Fig. 14.— Plot of gas-phase Fe/H estimated from the the sum of the Fe^+/H^+ and $\text{Fe}^{++}/\text{H}^+$ ratios (see Table 10). The Fe^+/H^+ ratios are derived using the $[\text{Fe II}] 26 \mu\text{m}$ line, but we do not account for an unknown, significant PDR contribution (see text). Because of this, the Fe^+/H^+ ratios are upper limits. This causes the Fe/H ratio here to be *overestimated*. However, since Fe^{3+} has not been accounted for, that would *increase* an assessment of gas-phase Fe/H (see text).

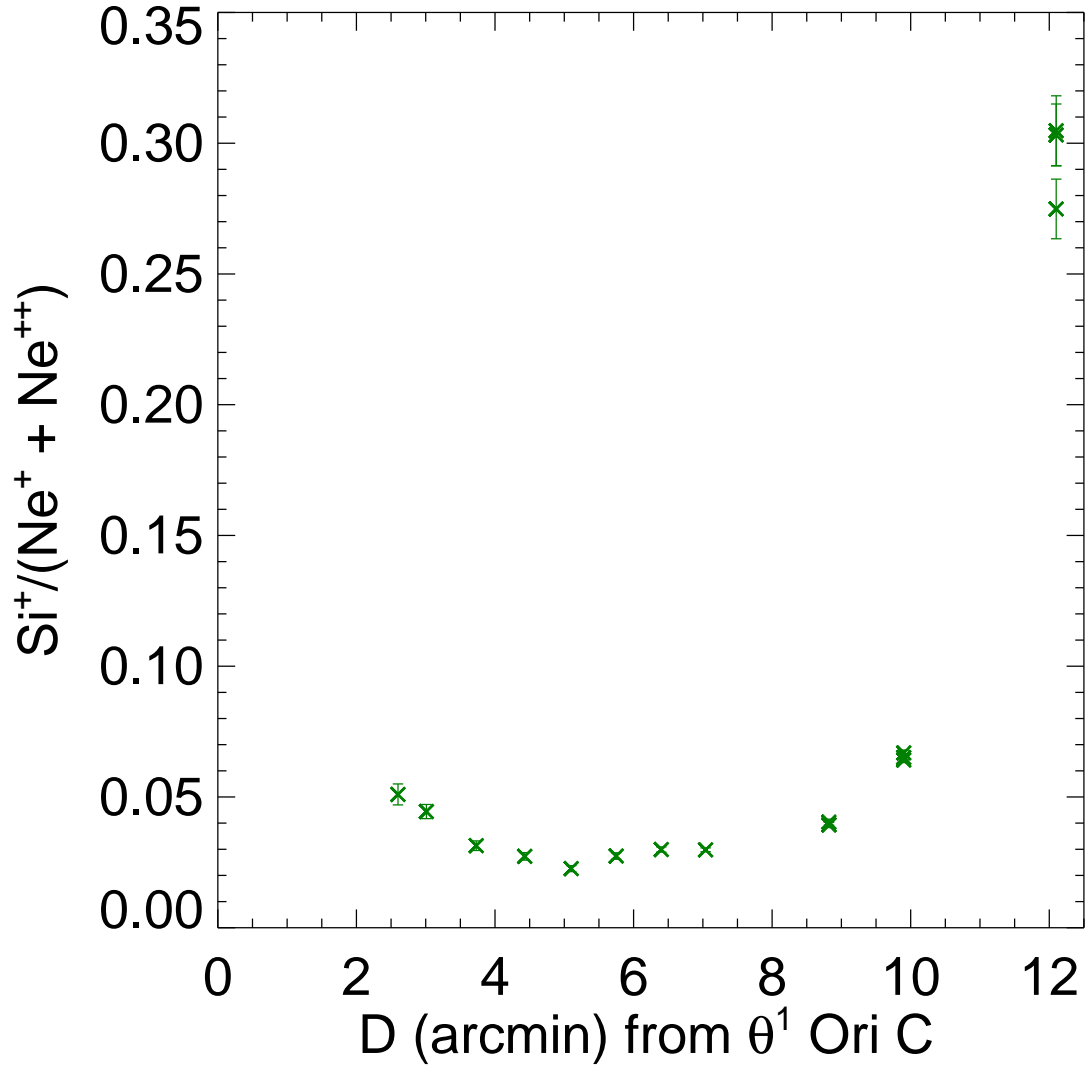


Fig. 15.— Plot of Si^+/Ne . This ratio is derived using the $[\text{Si II}]$ $34.8 \mu\text{m}$ line assuming that it is produced in the ionized region *only* and does not account for an unknown, significant PDR contribution (see text). The large increase at the outermost V3 position is strong evidence that the bulk of the $[\text{Si II}]$ 34.8 emission arises in a PDR at this H II region – PDR interface.

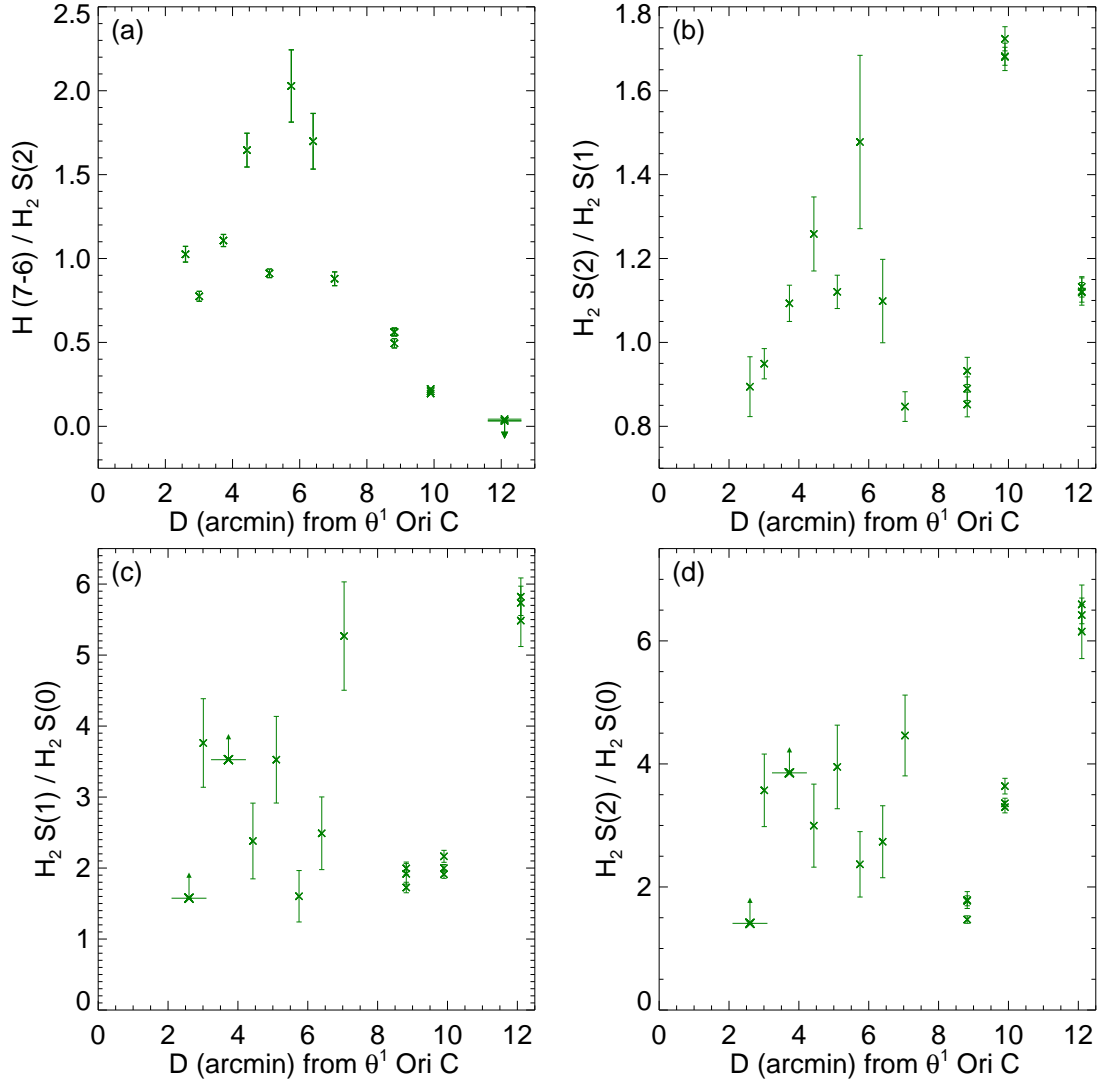


Fig. 16.— This plots the flux ratio versus D of the $H(7-6)$ line, which arises in the H II region, to the three H_2 lines, which arise in the PDR. (a) $H(7-6)/H_2 S(2)$; (b) $H_2 S(2)/H_2 S(1)$; (c) $H_2 S(1)/H_2 S(0)$; and (d) $H_2 S(2)/H_2 S(0)$.

Table 1. Regions Observed in M42

Chex	Distance (arcmin)	RA (J2000)	DEC
I4	2.60	5 35 23.3	-5 25 20.7
I3	3.01	5 35 24.4	-5 25 39.1
I2	3.73	5 35 26.3	-5 26 12.1
I1	4.43	5 35 28.1	-5 26 43.8
M1	5.10	5 35 29.9	-5 27 14.4
M2	5.75	5 35 31.6	-5 27 43.6
M3	6.40	5 35 33.3	-5 28 12.9
M4	7.04	5 35 35.0	-5 28 42.1
V1	8.82	5 35 39.7	-5 30 2.7
V2	9.90	5 35 42.5	-5 30 51.9
V3	12.08	5 35 48.3	-5 32 30.3

Table 2. M42 *Spitzer* Line Measurements

Chex	Species	Line (μm)	Intensity ($\text{ergs cm}^{-2} \text{ s}^{-1}$)	1σ error (arcsec^{-2})	FWHM (km s^{-1})	V_{helio} (km s^{-1})
I4	[S IV]	10.5	2.48E-14	4.84E-16	483	11
	H ₂ S(2)	12.3	5.42E-15	1.98E-16	464	-44
	H I 7-6	12.4	5.56E-15	1.52E-16	474	-38
	[Ne II]	12.8	3.18E-13	1.27E-15	449	-60
	[Ne III]	15.6	5.53E-14	4.31E-16	451	-33
	H ₂ S(1)	17.0	6.06E-15	4.29E-16	491	-22
	[S III]	18.7	3.31E-13	2.40E-15	485	-11
	[Fe III]	22.9	1.12E-14	1.50E-15	539	-32
	[Fe II]	26.0	7.43E-15	6.21E-16	306	-81
	H ₂ S(0)	28.2	3.85E-15 ^a	—	—	—
	[S III]	33.5	2.39E-13	4.05E-15	448	-75
	[Si II]	34.8	8.92E-14	7.00E-15	554	-38
	I3	[S IV]	10.5	1.03E-14	2.03E-16	507
H ₂ S(2)		12.3	4.66E-15	1.15E-16	467	-42
H I 7-6		12.4	3.61E-15	1.05E-16	490	-25
[Ne II]		12.8	2.02E-13	8.54E-16	449	-49
[Ne III]		15.6	2.80E-14	1.92E-16	451	-27
H ₂ S(1)		17.0	4.91E-15	1.41E-16	462	11
[S III]		18.7	2.12E-13	1.60E-15	486	1
[Fe III]		22.9	5.95E-15	5.02E-16	524	-50
[Fe II]		26.0	5.05E-15	2.83E-16	473	-93
H ₂ S(0)		28.2	1.30E-15	2.13E-16	332	0
[S III]		33.5	1.87E-13	2.04E-15	450	-101
[Si II]		34.8	5.93E-14	3.62E-15	536	-63
I2		[S IV]	10.5	5.02E-15	1.31E-16	484
	H ₂ S(2)	12.3	2.76E-15	6.88E-17	459	-46
	H I 7-6	12.4	3.05E-15	6.40E-17	493	-30
	[Ne II]	12.8	1.71E-13	6.26E-16	446	-54
	[Ne III]	15.6	1.44E-14	1.27E-16	453	-32
	H ₂ S(1)	17.0	2.52E-15	7.72E-17	454	19
	[S III]	18.7	1.79E-13	1.21E-15	485	-1
	[Fe III]	22.9	6.01E-15	2.36E-16	438	-9
	[Fe II]	26.0	3.96E-15	1.80E-16	395	-99
	H ₂ S(0)	28.2	7.15E-16 ^a	—	—	—
	[S III]	33.5	1.65E-13	1.65E-15	452	-75
	[Si II]	34.8	3.62E-14	2.12E-15	536	-54
	I1	[S IV]	10.5	2.61E-15	1.12E-16	482
H ₂ S(2)		12.3	1.33E-15	6.95E-17	495	-34
H I 7-6		12.4	2.20E-15	7.06E-17	503	-15
[Ne II]		12.8	1.17E-13	2.01E-15	439	-58
[Ne III]		15.6	8.14E-15	9.86E-17	450	-35
H ₂ S(1)		17.0	2.52E-15	7.72E-17	454	19

Table 2—Continued

Chex	Species	Line (μm)	Intensity ($\text{ergs cm}^{-2} \text{ s}^{-1}$)	1σ error (arcsec^{-2})	FWHM (km s^{-1})	V_{helio} (km s^{-1})
	[S III]	18.7	1.25E-13	8.92E-16	488	0
	[Fe III]	22.9	4.80E-15	1.23E-16	483	-36
	[Fe II]	26.0	1.75E-15	7.92E-17	466	-96
	H ₂ S(0)	28.2	4.45E-16	9.75E-17	412	37
	[S III]	33.5	1.29E-13	1.25E-15	450	-93
	[Si II]	34.8	2.37E-14	1.20E-15	521	-60
M1	[S IV]	10.5	2.00E-15	6.90E-17	480	8
	H ₂ S(2)	12.3	1.70E-15	3.60E-17	474	-41
	H I 7-6	12.4	1.55E-15	2.89E-17	477	-20
	[Ne II]	12.8	8.37E-14	2.69E-16	441	-67
	[Ne III]	15.6	7.30E-15	6.59E-17	450	-42
	H ₂ S(1)	17.0	1.52E-15	4.33E-17	433	28
	[S III]	18.7	8.92E-14	5.41E-16	482	-8
	[Fe III]	22.9	3.23E-15	5.32E-17	426	7
	[Fe II]	26.0	1.17E-15	5.03E-17	486	-40
	H ₂ S(0)	28.2	4.31E-16	7.36E-17	400	13
	[S III]	33.5	1.01E-13	4.75E-16	453	-32
	[Si II]	34.8	1.53E-14	7.81E-16	529	11
M2	[S IV]	10.5	9.80E-16	4.28E-17	474	1
	H ₂ S(2)	12.3	5.47E-16	5.32E-17	771	11
	H I 7-6	12.4	1.11E-15	4.73E-17	508	-27
	[Ne II]	12.8	5.62E-14	2.08E-16	442	-71
	[Ne III]	15.6	3.80E-15	3.72E-17	452	-44
	H ₂ S(1)	17.0	3.70E-16	3.72E-17	500	39
	[S III]	18.7	5.90E-14	3.52E-16	482	-13
	[Fe III]	22.9	2.27E-15	5.30E-17	432	-3
	[Fe II]	26.0	9.21E-16	4.29E-17	454	-68
	H ₂ S(0)	28.2	2.31E-16	4.68E-17	431	25
	[S III]	33.5	7.24E-14	7.39E-16	439	-75
	[Si II]	34.8	1.33E-14	5.53E-16	512	-35
M3	[S IV]	10.5	5.00E-16	3.52E-17	477	21
	H ₂ S(2)	12.3	5.16E-16	3.94E-17	557	-22
	H I 7-6	12.4	8.76E-16	5.33E-17	540	-34
	[Ne II]	12.8	4.20E-14	5.18E-16	443	-60
	[Ne III]	15.6	2.11E-15	2.75E-17	459	-29
	H ₂ S(1)	17.0	4.70E-16	2.28E-17	333	56
	[S III]	18.7	4.64E-14	1.03E-16	488	1
	[Fe III]	22.9	2.11E-15	3.54E-17	425	0
	[Fe II]	26.0	6.93E-16	2.84E-17	443	-62
	H ₂ S(0)	28.2	1.89E-16	3.77E-17	448	36
	[S III]	33.5	5.87E-14	6.50E-16	443	-55
	[Si II]	34.8	1.12E-14	3.53E-16	509	-18

Table 2—Continued

Chex	Species	Line (μm)	Intensity ($\text{ergs cm}^{-2} \text{ s}^{-1}$)	1σ error (arcsec^{-2})	FWHM (km s^{-1})	V_{helio} (km s^{-1})
M4	[S IV]	10.5	3.44E-16	4.68E-17	601	-34
	H ₂ S(2)	12.3	6.76E-16	2.34E-17	473	-25
	H I 7-6	12.4	5.94E-16	1.85E-17	486	-23
	[Ne II]	12.8	3.33E-14	1.18E-16	442	-64
	[Ne III]	15.6	1.05E-15	1.75E-17	453	-35
	H ₂ S(1)	17.0	7.98E-16	1.86E-17	425	35
	[S III]	18.7	3.44E-14	2.25E-16	485	-1
	[Fe III]	22.9	1.53E-15	2.95E-17	475	-37
	[Fe II]	26.0	4.95E-16	2.39E-17	483	-96
	H ₂ S(0)	28.2	1.51E-16	2.17E-17	426	-35
	[S III]	33.5	4.42E-14	4.04E-16	448	-96
	[Si II]	34.8	8.88E-15	2.18E-16	503	-67
	V1-1	[S IV]	10.5	6.54E-17	3.66E-18	331
H ₂ S(2)		12.3	3.47E-16	8.14E-18	442	-40
H I 7-6		12.4	1.96E-16	6.93E-18	503	5
[Ne II]		12.8	1.11E-14	3.83E-17	444	-65
[Ne III]		15.6	3.03E-16	8.03E-18	464	-22
H ₂ S(1)		17.0	3.90E-16	8.26E-18	464	25
[Fe II]		17.9	3.00E-17	4.89E-18	487	103
[S III]		18.7	9.51E-15	3.78E-17	487	-1
[Fe III]		22.9	3.61E-16	1.28E-17	460	-15
[Fe II]		26.0	2.36E-16	1.33E-17	521	-88
H ₂ S(0)		28.2	1.96E-16	7.70E-18	406	-50
[S III]		33.5	1.37E-14	1.18E-16	440	-84
[Si II]		34.8	4.31E-15	1.17E-16	499	-52
V1-2	[S IV]	10.5	1.01E-16	1.18E-17	503	-77
	H ₂ S(2)	12.3	3.44E-16	7.99E-18	425	-52
	H I 7-6	12.4	1.93E-16	5.68E-18	493	-19
	[Ne II]	12.8	1.13E-14	4.22E-17	448	-80
	[Ne III]	15.6	3.21E-16	5.69E-18	461	-53
	H ₂ S(1)	17.0	4.04E-16	1.03E-17	454	13
	[Fe II]	17.9	3.42E-17	5.90E-18	416	90
	[S III]	18.7	9.59E-15	5.86E-17	488	-18
	[Fe III]	22.9	3.38E-16	1.16E-17	453	-4
	[Fe II]	26.0	2.18E-16	6.52E-18	449	-79
	H ₂ S(0)	28.2	2.34E-16	8.03E-18	414	-18
	[S III]	33.5	1.39E-14	1.33E-16	436	-84
	[Si II]	34.8	4.41E-15	1.09E-16	495	-53
V1-3	[S IV]	10.5	1.19E-16	2.84E-17	722	-9
	H ₂ S(2)	12.3	3.68E-16	9.68E-18	474	-39
	H I 7-6	12.4	1.82E-16	8.96E-18	461	-17

Table 2—Continued

Chex	Species	Line (μm)	Intensity ($\text{ergs cm}^{-2} \text{s}^{-1}$)	1σ error (arcsec^{-2})	FWHM (km s^{-1})	V_{helio} (km s^{-1})
	[Ne II]	12.8	1.11E-14	1.33E-16	440	-70
	[Ne III]	15.6	2.94E-16	4.92E-18	454	-41
	H ₂ S(1)	17.0	3.95E-16	8.95E-18	446	25
	[Fe II]	17.9	3.12E-17	8.61E-18	429	124
	[S III]	18.7	9.51E-15	5.80E-17	483	-7
	[Fe III]	22.9	3.60E-16	2.06E-17	460	12
	[Fe II]	26.0	2.49E-16	1.48E-17	466	-39
	H ₂ S(0)	28.2	2.06E-16	1.48E-17	395	-32
	[S III]	33.5	1.42E-14	1.69E-16	445	-54
	[Si II]	34.8	4.59E-15	1.20E-16	504	-18
V2-1	[S IV]	10.5	1.03E-16	5.76E-18	485	72
	H ₂ S(2)	12.3	1.21E-15	7.38E-18	442	-46
	H I 7-6	12.4	2.52E-16	1.09E-17	508	8
	[Ne II]	12.8	1.45E-14	5.00E-17	444	-68
	[Ne III]	15.6	1.76E-16	6.46E-18	473	-36
	H ₂ S(1)	17.0	7.18E-16	1.32E-17	461	24
	[Fe II]	17.9	1.21E-16	9.98E-18	545	59
	[S III]	18.7	8.19E-15	4.91E-17	487	-8
	[Fe III]	22.9	2.73E-16	9.90E-18	458	14
	[Fe II]	26.0	5.42E-16	1.06E-17	470	-30
	H ₂ S(0)	28.2	3.32E-16	1.14E-17	416	-11
	[S III]	33.5	1.09E-14	5.13E-17	450	-31
	[Si II]	34.8	8.87E-15	1.44E-16	506	11
V2-2	[S IV]	10.5	1.02E-16	7.95E-18	534	-55
	H ₂ S(2)	12.3	1.24E-15	7.91E-18	433	-38
	H I 7-6	12.4	2.43E-16	6.97E-18	477	6
	[Ne II]	12.8	1.49E-14	4.58E-17	440	-62
	[Ne III]	15.6	1.65E-16	2.69E-18	424	-54
	H ₂ S(1)	17.0	7.36E-16	8.13E-18	451	39
	[Fe II]	17.9	1.15E-16	9.91E-18	541	47
	[S III]	18.7	8.47E-15	1.13E-16	482	1
	[Fe III]	22.9	3.01E-16	1.13E-17	421	2
	[Fe II]	26.0	4.92E-16	5.37E-18	423	-47
	H ₂ S(0)	28.2	3.69E-16	8.66E-18	412	-8
	[S III]	33.5	1.13E-14	1.21E-16	445	-46
	[Si II]	34.8	8.89E-15	1.17E-16	501	-5
V2-3	[S IV]	10.5	9.37E-17	1.32E-17	692	-84
	H ₂ S(2)	12.3	1.19E-15	1.05E-17	444	-45
	H I 7-6	12.4	2.65E-16	6.69E-18	546	-38
	[Ne II]	12.8	1.46E-14	5.81E-17	443	-67
	[Ne III]	15.6	1.59E-16	5.51E-18	434	-54
	H ₂ S(1)	17.0	6.92E-16	9.84E-18	464	24

Table 2—Continued

Chex	Species	Line (μm)	Intensity ($\text{ergs cm}^{-2} \text{ s}^{-1}$)	1σ error (arcsec^{-2})	FWHM (km s^{-1})	V_{helio} (km s^{-1})
	[Fe II]	17.9	1.07E-16	6.82E-18	483	81
	[S III]	18.7	8.21E-15	4.92E-17	486	-7
	[Fe III]	22.9	2.90E-16	4.09E-17	462	-20
	[Fe II]	26.0	5.08E-16	9.48E-18	431	-70
	H ₂ S(0)	28.2	3.62E-16	9.67E-18	418	-63
	[S III]	33.5	1.15E-14	9.75E-17	450	-91
	[Si II]	34.8	8.96E-15	1.35E-16	500	-56
V3-1	[S IV]	10.5	2.15E-17 ^a	—	—	—
	H ₂ S(2)	12.3	1.55E-15	2.84E-17	421	-50
	H I 7-6	12.4	6.63E-17 ^a	—	—	—
	[Ne II]	12.8	1.47E-15	4.40E-17	446	-52
	[Ne III]	15.6	8.50E-17	4.78E-18	442	-18
	H ₂ S(1)	17.0	1.37E-15	1.52E-17	461	20
	[S III]	18.7	6.81E-16	1.32E-17	458	23
	[Fe III]	22.9	2.48E-17 ^a	—	—	—
	[Fe II]	26.0	4.15E-16	1.82E-17	478	-100
	H ₂ S(0)	28.2	2.35E-16	1.03E-17	396	-55
	[S III]	33.5	1.20E-15	2.43E-17	401	-134
	[Si II]	34.8	5.37E-15	1.76E-16	513	-66
V3-2	[S IV]	10.5	5.12E-17	8.90E-18	384	-34
	H ₂ S(2)	12.3	1.63E-15	2.84E-17	422	-53
	H I 7-6	12.4	5.40E-17 ^a	—	—	—
	[Ne II]	12.8	1.42E-15	4.19E-17	445	-58
	[Ne III]	15.6	7.88E-17	4.40E-18	345	-71
	H ₂ S(1)	17.0	1.45E-15	1.68E-17	461	17
	[S III]	18.7	6.54E-16	9.78E-18	460	14
	[Fe III]	22.9	4.11E-17 ^a	—	—	—
	[Fe II]	26.0	4.01E-16	1.86E-17	465	-98
	H ₂ S(0)	28.2	2.53E-16	9.94E-18	411	-41
	[S III]	33.5	1.24E-15	2.31E-17	396	-130
	[Si II]	34.8	5.44E-15	1.43E-16	515	-65
V3-3	[S IV]	10.5	7.54E-17 ^a	—	—	—
	H ₂ S(2)	12.3	1.54E-15	4.22E-17	419	-54
	H I 7-6	12.4	4.94E-17 ^a	—	—	—
	[Ne II]	12.8	1.51E-15	4.84E-17	449	-54
	[Ne III]	15.6	7.88E-17	4.66E-18	352	-71
	H ₂ S(1)	17.0	1.38E-15	1.31E-17	465	17
	[S III]	18.7	6.95E-16	1.02E-17	465	21
	[Fe III]	22.9	5.80E-17 ^a	—	—	—
	[Fe II]	26.0	4.15E-16	2.06E-17	470	-87
	H ₂ S(0)	28.2	2.51E-16	1.65E-17	437	-57
	[S III]	33.5	1.40E-15	3.69E-17	493	-119

Table 2—Continued

Chex	Species	Line (μm)	Intensity ($\text{ergs cm}^{-2} \text{ s}^{-1} \text{ arcsec}^{-2}$)	1σ error (arcsec^{-2})	FWHM (km s^{-1})	V_{helio} (km s^{-1})
	[Si II]	34.8	5.51E-15	1.51E-16	521	-69

^a Intensity less than 3σ , considered an upper limit

Table 3. Surface Brightness and Extinction Values

Sample Name	Distance (arcmin)	$c_{H\beta}$	$S(H\beta)$ (corrected) (ergs cm ⁻² s ⁻¹ arcsec ⁻²)	Comments
I4-S120	2.91	0.19	2.97×10^{-13}	—
I3-JW831	3.51	0.21	2.52×10^{-13}	—
I2I3-S150	3.48	0.14	2.09×10^{-13}	—
I2-JW831	3.95	0.20	2.16×10^{-13}	—
I1I2-S180	4.50	0.10	1.39×10^{-13}	—
I1I2-JW831	4.47	0.23	2.05×10^{-13}	—
M1M2M3-JW831	5.64	0.15	8.99×10^{-14}	—
M4	7.04	0.05	4.80×10^{-14}	—
V1	8.82	0.03	1.88×10^{-14}	—
V2-JW873-NE	10.59	0.11	2.30×10^{-14}	—
V2-JW887-E	10.94	0.13	2.07×10^{-14}	—
V2	10.44	0	1.47×10^{-14}	$H\alpha/H\beta=2.82$
V2-JW887-W	9.86	0	1.93×10^{-14}	$H\alpha/H\beta=2.82$
V2-JW887-WW	9.47	0	1.17×10^{-14}	$H\alpha/H\beta=2.73$
V2-JW873-SW	10.34	0	1.73×10^{-14}	$H\alpha/H\beta=2.78$
V3	12.10	0.11	1.52×10^{-14}	—

Note. — $c_{H\beta}$ is derived from the Blagrove et al. (2007) extinction curve, the observed $H\alpha/H\beta$ ratio and an assumed intrinsic ratio of 2.89, appropriate for the range of electron temperatures and densities in this paper.

Table 4. Observed and Extinction Corrected Line Ratios-1

Region λ (\AA)	Ion	I4-S120		I3-JW831		I213-S150		I2-JW831	
		F_λ	I_λ	F_λ	I_λ	F_λ	I_λ	F_λ	I_λ
3869	[Ne III]	0.0337	0.0359			0.0268	0.0278		
4070	[S II]	0.0123	0.0130			0.0145	0.0151		
4102	H I	0.215	0.226			0.225	0.234		
4340	H I	0.437	0.454	0.456	0.478	0.450	0.463	0.438	0.456
4363	[O III]	0.0035	0.0036	0.0068	0.0071				
4471	He I	0.0272	0.0280	0.0284	0.0293	0.0322	0.0329	0.0342	0.0352
4658	[Fe III]	0.0077	0.0078	0.0088	0.0089	0.0108	0.0109	0.0113	0.0115
4861	H I	1.000	1.000	1.000	1.000	1.000	1.000	1.000	1.000
4922	He I	0.0068	0.0068	0.0053	0.0053	0.0083	0.0083	0.0085	0.0085
4959	[O III]	0.326	0.324	0.355	0.352	0.316	0.315	0.283	0.281
5007	[O III]	0.997	0.987	1.066	1.055	0.960	0.953	0.939	0.930
5048	He I			0.0056	0.0055				
5056	Si II			0.0036	0.0035	0.0027	0.0027	0.0023	0.0023
5199	[N I]	0.0073	0.0072	0.0069	0.0067	0.0082	0.0081	0.0066	0.0064
5270	[Fe III]	0.0052	0.0051	0.0048	0.0047	0.0048	0.0047	0.0063	0.0061
5518	[Cl III]	0.0037	0.0035	0.0037	0.0035	0.0046	0.0045	0.0043	0.0041
5538	[Cl III]	0.0025	0.0024	0.0030	0.0029	0.0048	0.0047	0.0044	0.0042
5755	[N II]	0.0076	0.0072	0.0072	0.0068	0.0065	0.0062	0.0062	0.0059
5876	He I	0.0951	0.0895	0.0943	0.0882	0.102	0.0976	0.106	0.0998
5979	Si II	0.0018	0.0017	0.0018	0.0017			0.0018	0.0017
6300	[O I]	0.0060	0.0055	0.0063	0.0057	0.0045	0.0042	0.0044	0.0040
6312	[S III]	0.0109	0.0100	0.0115	0.0105	0.0115	0.0108	0.0123	0.0113
6347	Si II	0.0039	0.0036	0.0036	0.0033	0.0026	0.0025	0.0031	0.0028
6363	[O I]	0.0022	0.0020	0.0025	0.0023			0.0014	0.0013
6371	Si II	0.0030	0.0028	0.0026	0.0024			0.0036	0.0033
6548	[N II]	0.347	0.315	0.282	0.254	0.304	0.283	0.275	0.249
6563	H I	3.188	2.895	3.210	2.886	3.097	2.885	3.198	2.890
6583	[N II]	0.913	0.828	0.913	0.820	0.833	0.775	0.805	0.727
6678	He I	0.0265	0.0239	0.0264	0.0236	0.0305	0.0283	0.0300	0.0269
6716	[S II]	0.126	0.113	0.129	0.115	0.122	0.113	0.120	0.108
6731	[S II]	0.147	0.132	0.143	0.127	0.127	0.118	0.123	0.110
7065	He I	0.0285	0.0252			0.0392	0.0358		
7136	[Ar III]	0.0838	0.0739			0.0924	0.0843		

Table 5. Observed and Extinction Corrected Line Ratios-2

Region λ (\AA)	Ion	I12-S180		I12-JW831		M1M2M3-JW831	
		F_λ	I_λ	F_λ	I_λ	F_λ	I_λ
3869	[Ne III]	0.0365	0.0377				
4070	[S II]	0.0233	0.0229				
4102	H I	0.222	0.228				
4340	H I	0.434	0.433	0.420	0.455	0.433	0.466
4363	[O III]	0.0068	0.0069				
4471	He I	0.0336	0.0341	0.0310	0.0321	0.0278	0.0284
4658	[Fe III]	0.0098	0.0099	0.0092	0.0093	0.0082	0.0083
4861	H I	1.000	1.000	1.000	1.000	1.000	1.000
4922	He I	0.0081	0.0081	0.0053	0.0053	0.0079	0.0079
4959	[O III]	0.318	0.318	0.287	0.285	0.283	0.282
5007	[O III]	0.867	0.863	0.877	0.867	0.848	0.842
5042	Si II			0.0063	0.0063	0.0022	0.0022
5056	Si II			0.0044	0.0043	0.0042	0.0041
5199	[N I]	0.0068	0.0067	0.0050	0.0049	0.0069	0.0068
5270	[Fe III]			0.0060	0.0058	0.0057	0.0056
5518	[Cl III]	0.0033	0.0032	0.0050	0.0048	0.0038	0.0037
5538	[Cl III]	0.0033	0.0032	0.0042	0.0040	0.0038	0.0037
5755	[N II]	0.0075	0.0073	0.0070	0.0066	0.0073	0.0070
5876	He I	0.103	0.0993	0.0995	0.0925	0.0883	0.0842
5979	Si II					0.0019	0.0018
6300	[O I]	0.0052	0.0050	0.0032	0.0029	0.0023	0.0022
6312	[S III]	0.0106	0.0101	0.0119	0.0108	0.0116	0.0109
6347	Si II	0.0033	0.0032	0.0035	0.0032	0.0024	0.0022
6363	[O I]	0.0014	0.0013	0.0012	0.0011	0.0010	0.0009
6371	Si II	0.0031	0.0030	0.0029	0.0026	0.0020	0.0019
6548	[N II]	0.352	0.335	0.325	0.290	0.330	0.306
6563	H I	3.052	2.901	3.256	2.909	3.120	2.892
6583	[N II]	0.849	0.807	0.895	0.855	0.952	0.882
6678	He I	0.0310	0.0294	0.0278	0.0246	0.0234	0.0216
6716	[S II]	0.123	0.120	0.154	0.136	0.153	0.141
6731	[S II]	0.117	0.111	0.154	0.136	0.138	0.127
7065	He I	0.0286	0.0269				
7136	[Ar III]	0.0893	0.0837				

Table 6. Observed and Extinction Corrected Line Ratios-3 Near Position V2*

Region λ (Å)	Ion	JW873-NE		JW887-E		V2	JW887-W	JW887-WW	JW873-SW
		F_λ	I_λ	F_λ	I_λ	F_λ	F_λ	F_λ	F_λ
4340	H I	0.443	0.453	0.448	0.460	0.438	0.466	0.469	0.456
4363	[O III]					0.0158			
4471	He I	0.0282	0.0287	0.0270	0.0275	0.0200	0.0115	0.0130	0.0091
4658	[Fe III]	0.0082	0.0083	0.0072	0.0073	0.0052	0.0088	0.0097	0.0073
4861	H I	1.000	1.000	1.000	1.000	1.000	1.000	1.000	1.000
4922	He I	0.0055	0.0055	0.0048	0.0048	0.0057	0.0019	0.0027	0.0035
4959	[O III]	0.490	0.488	0.505	0.503	0.410	0.197	0.282	0.175
4986	[Fe III]						0.0034	0.0041	0.0049
5007	[O III]	1.622	1.613	1.640	1.629	1.223	0.579	0.819	0.518
5042	Si II					0.0079	0.026		0.0035
5056	Si II					0.0046	0.0030		0.0018
5199	[N I]	0.0305	0.0301	0.0286	0.0281	0.0598	0.0270	0.0150	0.0278
5262	[Fe II]	0.0025	0.0025	0.0021	0.0021	0.0045	0.0023		0.0023
5270	[Fe III]	0.0063	0.0062	0.0066	0.0065	0.0079	0.055	0.0047	0.0054
5518	[Cl III]	0.0040	0.0039	0.0057	0.0044	0.0041	0.0039	0.0047	0.0040
5538	[Cl III]	0.0030	0.0029	0.0057	0.0054	0.0039	0.0031	0.0038	0.0025
5755	[N II]	0.0103	0.0100	0.0109	0.0105	0.0103	0.0153	0.0152	0.0142
5876	He I	0.0925	0.0871	0.0977	0.0933	0.0675	0.0314	0.0443	0.0300
5979	Si II	0.0029	0.0028	0.0022	0.0021	0.0048	0.0024	0.0020	0.0027
6046	O I	0.0019	0.0018	0.0014	0.0013	0.0038			0.0014
6300	[O I]	0.0112	0.0107	0.0130	0.0123	0.0246	0.0433		0.0293
6312	[S III]	0.0144	0.0137	0.0152	0.0144	0.0135	0.0136		0.0125
6347	Si II	0.0038	0.0036	0.0043	0.0041	0.0061	0.0042	0.0026	0.0031
6363	[O I]	0.0036	0.0034	0.0043	0.0041	0.0077	0.0136	0.006	0.0088
6371	Si II	0.0034	0.0032	0.0033	0.0031	0.0055	0.0036	0.0020	0.0033
6548	[N II]	0.366	0.346	0.356	0.344	0.375	0.488	0.413	0.477
6563	H I	3.106	2.938	3.065	2.870	2.821	2.816	2.734	2.780
6583	[N II]	1.065	0.994	0.972	0.910	1.083	1.468	1.150	1.457
6678	He I	0.0255	0.0241	0.0267	0.0249	0.0204	0.0075	0.0098	0.0071
6716	[S II]	0.212	0.200	0.211	0.196	0.282	0.510	0.221	0.459
6731	[S II]	0.176	0.169	0.190	0.177	0.227	0.422	0.175	0.362

Note. — *Where only the observed flux ratios (F_λ) are shown, no extinction could be determined since the $H\alpha/H\beta$ ratio was less than the theoretically expected value.

Table 7. Observed and Extinction Corrected Line Ratios-4 2009 Observations

Region λ (\AA)	Ion	M4		V1		V3	
		F_λ	I_λ	F_λ	I_λ	F_λ	I_λ
3869	[Ne III]	0.0405	0.0412	0.0439	0.0443	0.1050	0.1091
4070	[S II]	0.0157	0.0159	0.0251	0.0253	0.0304	0.0314
4102	H I	0.2307	0.2340	0.2418	0.2436	0.2204	0.2273
4340	H I	0.4470	0.4516	0.4550	0.4574	0.4213	0.4309
4363	[O III]	0.0020	0.0020	0.0048	0.0048	0.0116	0.0119
4471	He I	0.0256	0.0258	0.0120	0.0120	0.0271	0.0276
4658	[Fe III]	0.0084	0.0084	0.0089	0.0089	0.0076	0.0077
4861	H I	1.000	1.000	1.000	1.000	1.000	1.000
4922	He I	0.0057	0.0057	0.0033	0.0033	0.0046	0.0046
4959	[O III]	0.2029	0.2025	0.1926	0.1924	0.6034	0.6010
5007	[O III]	0.6269	0.6253	0.5917	0.5925	1.8118	1.8010
5199	[N I]	0.0084	0.0083	0.0198	0.0198	0.0269	0.0265
5270	[Fe III]	0.0052	0.0051	0.0053	0.0053	0.0032	0.0031
5518	[Cl III]	0.0045	0.0045	0.0030	0.0030	0.0052	0.0051
5538	[Cl III]	0.0029	0.0029	0.0024	0.0024	0.0036	0.0035
5755	[N II]	0.0085	0.0084	0.0141	0.0140	0.0102	0.0097
5876	He I	0.0791	0.0778	0.0377	0.0374	0.1080	0.1042
5979	Si II	0.0018	0.0018	0.0025	0.0025	0.0039	0.0037
6300	[O I]	0.0085	0.0083	0.0108	0.0107	0.0251	0.0239
6312	[S III]	0.0111	0.0109	0.0121	0.0120	0.0138	0.0131
6347	Si II	0.0018	0.0018	0.0024	0.0024	0.0032	0.0030
6363	[O I]	0.0024	0.0024	0.0028	0.0028	0.0084	0.0080
6371	Si II	0.0014	0.0014	0.0019	0.0019	0.0017	0.0016
6548	[N II]	0.3425	0.3337	0.4480	0.4420	0.2829	0.2672
6563	H I	2.9673	2.89	2.9292	2.89	3.0625	2.89
6583	[N II]	1.1022	1.0730	1.3934	1.3890	0.8438	0.7960
6678	He I	0.0205	0.0199	0.0108	0.0106	0.0320	0.0301
6716	[S II]	0.1669	0.1622	0.3105	0.3059	0.1759	0.1652
6731	[S II]	0.1394	0.1355	0.2387	0.2352	0.1509	0.1417
7065	He I	0.0188	0.0182	0.0129	0.0127	0.0401	0.0373
7136	[Ar III]	0.0617	0.0596	0.0346	0.0340	0.1145	0.1062

Table 8. Electron Densities and Temperatures Derived from Optical Lines

Sample Name	Distance (arcmin)	N_e [S II] (cm^{-3})	T_e [N II] (K)	T_e [O III] (K)
I4-S120	2.91	714	8270	8550
I3-JW831	3.51	586	8280	10150
I2I3-S150	3.48	478	8070	—
I2-JW831	3.95	434	8160	—
I1I2-S180	4.5	290	8310	10630
I1I2-JW831	4.47	404	7950	—
M1M2M3-JW831	5.64	256	8090	—
M4	7.04	168	8230	8280
V1	8.82	87	8930	10780
V2-JW873-NE	10.59	181	8890	—
V2-JW887-E	10.94	259	9260	—
V2-Combined	10.44	131	8880	13400
V2-JW887-W	9.86	158	9030	—
V2-JW887-WW	9.47	114	8970	—
V2-JW873-SW	10.34	111	8830	—
V3	12.08	197	9580	10100

Table 9. Electron Densities from [S III] Infrared Lines

Chex	N_e [S III] (cm^{-3})
I4	1041
I3	755
I2	698
I1	572
M1	487
M2	403
M3	378
M4	365
V1-1	276
V1-2	273
V1-3	249
V2-1	337
V2-2	335
V2-3	297
V3-1	143
V3-2	105
V3-3	74

Table 10. Derived Parameters for M42

Chex	$\frac{\text{Ne}^+}{\text{H}^+}$ ($\times 10^{-6}$)	$\frac{\text{Ne}^{++}}{\text{H}^+}$ ($\times 10^{-6}$)	$\frac{\text{S}^{++}}{\text{H}^+}$ ($\times 10^{-6}$)	$\frac{\text{S}^{3+}}{\text{H}^+}$ ($\times 10^{-8}$)	$\frac{\text{Ne}^{++}}{\text{Ne}^+}$ ($\times 10^{-3}$)	$\frac{\text{S}^{3+}}{\text{S}^{++}}$ ($\times 10^{-3}$)	$\frac{\text{Ne}^a}{\text{S}}$	$\frac{\text{Fe}^{++}}{\text{Fe}^+}$	$\frac{\text{Fe}^+}{\text{H}}$ ($\times 10^{-6}$)	$\frac{\text{Fe}^{++}}{\text{H}}$ ($\times 10^{-6}$)	$\frac{\text{Si}^+}{\text{Ne}}$ ($\times 10^{-2}$)
I4	101 ± 9	8.59 ± 0.76	6.66 ± 0.59	13.1 ± 1.2	84.8 ± 0.7	19.7 ± 0.4	16.2 ± 0.1	1.68 ± 0.26	0.584 ± 0.049	0.980 ± 0.131	5.10 ± 0.40
I3	99 ± 9	6.70 ± 0.60	6.58 ± 0.59	8.27 ± 0.75	67.4 ± 0.5	12.6 ± 0.3	15.9 ± 0.1	1.38 ± 0.14	0.573 ± 0.032	0.791 ± 0.067	4.44 ± 0.27
I2	100 ± 9	4.05 ± 0.35	6.59 ± 0.57	4.74 ± 0.43	40.7 ± 0.4	7.18 ± 0.19	15.6 ± 0.1	1.80 ± 0.11	0.523 ± 0.024	0.941 ± 0.037	3.14 ± 0.18
I1	95 ± 9	3.19 ± 0.29	6.50 ± 0.59	3.40 ± 0.34	33.7 ± 0.7	5.23 ± 0.23	15.0 ± 0.3	3.33 ± 0.17	0.311 ± 0.014	1.037 ± 0.027	2.73 ± 0.14
M1	96 ± 8.3	4.05 ± 0.35	6.60 ± 0.57	3.66 ± 0.34	42.2 ± 0.4	5.54 ± 0.19	15.1 ± 0.1	3.43 ± 0.16	0.286 ± 0.012	0.982 ± 0.016	2.26 ± 0.12
M2	89.1 ± 8.6	2.96 ± 0.28	6.21 ± 0.59	2.51 ± 0.26	33.2 ± 0.7	4.04 ± 0.18	14.8 ± 0.3	3.14 ± 0.16	0.306 ± 0.014	0.962 ± 0.023	2.74 ± 0.12
M3	85.5 ± 9	2.07 ± 0.22	6.23 ± 0.65	1.62 ± 0.20	24.3 ± 0.4	2.60 ± 0.18	14.0 ± 0.2	3.92 ± 0.17	0.289 ± 0.012	1.133 ± 0.019	2.99 ± 0.10
M4	100 ± 9	1.52 ± 0.14	6.84 ± 0.62	1.64 ± 0.27	15.2 ± 0.3	2.40 ± 0.33	14.8 ± 0.1	4.00 ± 0.21	0.303 ± 0.015	1.214 ± 0.023	2.98 ± 0.07
V1-1	101 ± 9	1.34 ± 0.13	5.89 ± 0.54	0.940 ± 0.100	13.2 ± 0.4	1.60 ± 0.09	17.4 ± 0.1	2.04 ± 0.14	0.423 ± 0.024	0.864 ± 0.031	3.94 ± 0.11
V1-2	105 ± 9	1.44 ± 0.13	6.04 ± 0.54	1.48 ± 0.22	13.7 ± 0.2	2.45 ± 0.29	17.6 ± 0.1	2.08 ± 0.09	0.396 ± 0.012	0.822 ± 0.028	3.93 ± 0.10
V1-3	109 ± 11	1.40 ± 0.14	6.40 ± 0.63	1.84 ± 0.48	12.8 ± 0.3	2.88 ± 0.69	17.3 ± 0.2	1.95 ± 0.16	0.475 ± 0.028	0.926 ± 0.053	4.04 ± 0.12
V2-1	103 ± 10	0.602 ± 0.061	3.86 ± 0.37	1.15 ± 0.13	5.86 ± 0.22	2.98 ± 0.17	26.7 ± 0.2	0.656 ± 0.027	0.773 ± 0.015	0.507 ± 0.018	6.69 ± 0.11
V2-2	110 ± 10	0.588 ± 0.053	4.15 ± 0.37	1.19 ± 0.14	5.35 ± 0.09	2.87 ± 0.23	26.5 ± 0.3	0.799 ± 0.031	0.729 ± 0.008	0.583 ± 0.022	6.51 ± 0.09
V2-3	98 ± 9	0.517 ± 0.049	3.73 ± 0.33	1.00 ± 0.17	5.26 ± 0.18	2.68 ± 0.38	26.5 ± 0.2	0.755 ± 0.107	0.677 ± 0.013	0.512 ± 0.072	6.41 ± 0.10
V3-1	≥ 40.0	≥ 1.11	≥ 1.33	—	27.9 ± 1.8	≤ 6.9	≥ 30.8	≤ 0.0851	≤ 2.05	—	30.5 ± 1.3
V3-2	≥ 47.4	≥ 1.27	≥ 1.60	≥ 2.67	26.8 ± 1.7	16.7 ± 2.9	29.9 ± 1.0	≤ 0.149	≤ 2.38	—	30.3 ± 1.2
V3-3	≥ 55.6	≥ 1.39	≥ 1.91	—	25.1 ± 1.7	≤ 22.5	≥ 29.2	≤ 0.207	≤ 2.64	—	27.5 ± 1.1

^a $(\text{Ne}^+ + \text{Ne}^{++}) / (\text{S}^{++} + \text{S}^{3+})$. See text for correction for S^+ .